



HAL
open science

A SIMP-Phase field topology optimization framework to maximize quasi-brittle fracture resistance of 2D and 3D composites

Pengfei Li, Yi Wu, Julien Yvonnet

► To cite this version:

Pengfei Li, Yi Wu, Julien Yvonnet. A SIMP-Phase field topology optimization framework to maximize quasi-brittle fracture resistance of 2D and 3D composites. *Theoretical and Applied Fracture Mechanics*, 2021, 114, pp.102919. 10.1016/j.tafmec.2021.102919 . hal-03225114

HAL Id: hal-03225114

<https://hal.science/hal-03225114v1>

Submitted on 12 May 2021

HAL is a multi-disciplinary open access archive for the deposit and dissemination of scientific research documents, whether they are published or not. The documents may come from teaching and research institutions in France or abroad, or from public or private research centers.

L'archive ouverte pluridisciplinaire **HAL**, est destinée au dépôt et à la diffusion de documents scientifiques de niveau recherche, publiés ou non, émanant des établissements d'enseignement et de recherche français ou étrangers, des laboratoires publics ou privés.

A SIMP-Phase field topology optimization framework to maximize quasi-brittle fracture resistance of 2D and 3D composites

Pengfei Li^a, Yi Wu^{a,b}, Julien Yvonnet^{a,*}

^a*MSME, Univ Gustave Eiffel, CNRS UMR 8208, F-77474 Marne-la-Vallée, France*

^b*State Key Laboratory of Advanced Design and Manufacturing for Vehicle Body, Hunan University, Changsha, 410082, China*

Abstract

We investigate the use of combining SIMP topology optimization and phase field method to fracture for maximizing the fracture resistance of a structure composed of two materials. The optimization problem is formulated with respect to maximizing the external work under the constraint of inclusion volume fraction. The performance and convergence of the proposed algorithm are investigated. It is shown that the fracture resistance can be improved as compared to several guess designs with the same volume fraction of reinforcement (inclusion material). A comparison between the present SIMP and BESO methods is performed, showing a better convergence of the SIMP method, more specifically when a homogeneous initial guess design is used. Applications to 2D and 3D composite structure are presented to show the potential and robustness of the approach.

Keywords: Fracture resistance, Topology optimization, SIMP, Phase field method, two-material structures, 3D applications

1. Introduction

Recently, design of composites with enhanced resistance to damage and fracture has emerged as a new challenging and exciting topic in computational mechanics. With the quick development of 3D printing and additive manufacturing techniques [46], new technological solutions which were not possible a few years ago can now be considered, like on-demand geometries of multi-materials structures and microstructures. More specifically, 3D printed bi-materials [7, 30–32, 63] offer new exciting possibilities such as designing composites with non-trivial periodic microstructures and ad-hoc functionalities. Among them, particle-matrix or skeleton-filled matrix composites able to increase the fracture resistance as compared to existing composites is of industrial and technological critical importance, for applications in aircraft, automotive or biomechanics, among many others.

One central ingredient for this task is the use of Topology Optimization (TO). TO has been widely studied and employed in both academic and engineering applications since it was firstly proposed by Bendsoe and Kikuchi [14]. It is generally accepted that topology optimization methods can be mainly categorized into three kinds of families, namely the Solid Isotropic Material with Penalization (SIMP) method [12, 13, 53], the level set method [3, 62], and the Evolutionary Structural Optimization (ESO) method [67]. Review of these methods can be found in state-of-the-art

*Corresponding author

Email address: julien.yvonnet@univ-paris-est.fr (Julien Yvonnet)

papers [22, 52, 61, 71]). An interesting comparison review on these techniques, with advantages and drawbacks, can be found in [59].

Initially mainly applied to maximize the stiffness of structures under volume constraints, TO has since then been extended and applied to a broad variety of problems like mechanical and thermal loads of structures, fluid flow, dynamics, acoustics and biomechanics, among many others (see a survey paper in [22]).

More recently, TO has been applied to enhance the mechanical resistance of structures and materials subjected to damage and cracking.

One pioneering work combining TO and fracture mechanics can be traced back to Challis et al. [19], where the level-set TO method has been used to maximize fracture resistance of structures, defined as the elastic energy released by the crack that are in tension and was calculated using the virtual crack extension. However, in this work, no real crack tips with stress singularity in the context of linear fracture mechanics were modeled. Another related technique can be found in [29], where pre-defined cracks were inserted and TO used to minimize the J-integral around crack tip singularity as a fracture criterion.

An important progress was made by optimizing the topology while taking into account the incremental damage response of the structure during a full load, from initiation to damaged/cracked structures. A first series of works have been proposed where damage mechanics was considered during the TO problem. In [8, 9], Amir and Sigmund used a gradient enhanced model to define the truss topology and optimal cross sections of reinforcement bars, and where the external work was maximized as an evaluation of the fracture energy. In [33], Kato and Ramm investigated optimal placement and shape of reinforcement in composites with respect to damage criterion to optimize the structural ductility during a full incremental procedure. In [26], Hilchenbach and Ramm optimized the position and shapes of stiff inclusions during the nonlinear loading of a structure. Even though not implying TO, the work shares similarities with the procedures developed in TO in this context. In [28], James and Waisman developed TO within a nonlocal damage framework using SIMP where TO was performed with respect to a maximum damage criterion during the whole nonlinear load of a structure while minimizing the quantity of material within the structure as an objective. In [38], Liu et al. investigated TO with respect to damage induced by debonding at the interfaces between two materials in a structure during an incremental loading with Level-set TO and XFEM description of interfaces location. In [34–36], Li et al. proposed SIMP TO using an elastoplastic-damage model where TO was performed to find the optimal structural topologies with high energy absorption capacity while constraining the damage indicator.

An important recent step was to include brittle fracture propagation [57, 65] within TO. In [69] Zhang et al. used TO with XFEM and took into account full crack propagation to optimize several indicators such as tensile stress during loading of a structure. One issue with XFEM as a crack propagation simulation tool is its complexity in 3D and its inability to initiate the cracks, as well as handling multiple, complex crack networks which may connect and merge during the process. The development of the variational approach to fracture [4, 16, 17, 23, 39, 42, 47, 49, 70], also called phase field method in the literature, offers several advantages in the context of crack propagation simulation, like: the possibility to initiate cracks from undamaged configurations; the possibility to handle arbitrary crack networks (including branching, merging, in both 2D and 3D) without specific treatment and use of classical finite elements; a variational framework allowing to include many models or mechanisms, and a mesh-independence due to an appropriate regularization process. This point is of special interest in TO approach where the use of a fixed mesh is required.

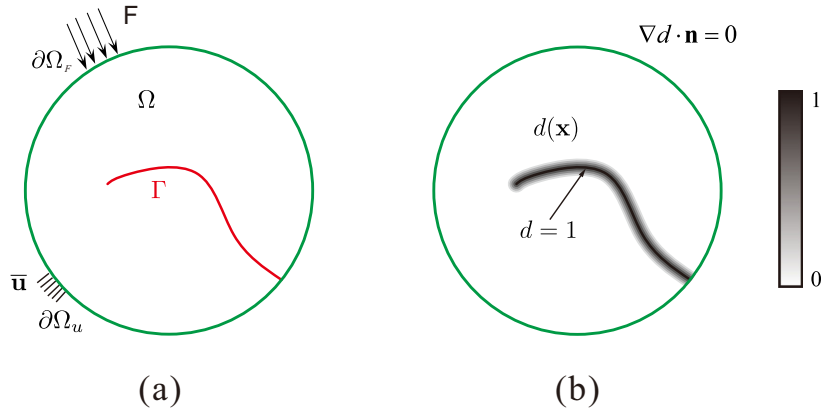


Figure 1: Phase field approximation of a sharp crack discontinuity. (a) A sharp crack surface Γ embedded into the solid Ω . (b) The regularized representation of the crack by the phase field $d(\mathbf{x})$.

In [56], San and Waisman combined phase field and genetic algorithms to find the optimal location of particles in order to maximize indicators such as the peak force, maximum deformation at failure point and maximum fracture energy during an incremental procedure. The first works to our knowledge combining phase field and TO was introduced in Xia et al. and Da et al. in [21, 66], where the BESO TO [27] was used to optimize the fracture resistance of two-phase structures with respect to inclusions shapes, including cracks in both bulk and interfaces, and applied to periodic composites and multiple loads in [20]. In [54, 55], Russ and Waisman developed a SIMP TO combined with phase field to optimize the fracture energy in one-phase material structures, and Wu et al. [64] developed a Level-Set TO-phase field approach to optimize the fracture resistance of composites.

In this work, we extend our previous BESO framework [66] to a combined SIMP and phase field for maximizing the fracture energy of two-phase composites. It is worth noting that the present framework shares many similarities with the recent framework of [54]: phase field and SIMP are combined for maximizing fracture resistance and the objective function used in both of these works include the external work computed incrementally during a full crack propagation simulation. The main contribution here is the application of the SIMP-phase field to two-material structures, where the objective here is not to minimize the total weight as in [54] but to modify the topology of a second phase material under the constraint of a volume fracture. Another contribution is a comparison of the present SIMP results with BESO formulations with respect to convergence and performance (value of objective function). Finally, the last contribution is applications of this framework to 3D 2-material structures which show the full potential of the approach.

The present paper is organized as follows. In Section 2, we review the phase field method for brittle fracture based on the variational framework and provide the details of the finite element discretization. In Section 3, we propose the SIMP topology optimization approach for the design of brittle composites to maximize the fracture resistance in two-phase composites. Section 4 provides the overall algorithms to practically implement the present framework. Finally, a series of 2D and 3D numerical examples are presented in Section 5 to show the efficiency and potential of the approach.

2. Phase field fracture formulation

In this work, we briefly review the phase field method for fracture which will serve as one main ingredient in the present topology optimization framework.

Let $\Omega \subset \mathbb{R}^D$ be an open domain with $D = 2, 3$, describing a cracked solid as depicted in Fig. 1. The external boundary of Ω is denoted by $\partial\Omega \in \mathbb{R}^{D-1}$. Cracks which may propagate within the solid are collectively denoted by Γ . In this work, we adopt the framework proposed in [6, 39, 41, 42] for a regularized representation of discontinuities. In this regularized framework, the crack is approximately represented by a scalar phase field $0 \leq d(\mathbf{x}, t) \leq 1$ (see Fig. 1(b)), such that when $d = 0$ the material is undamaged, and when $d = 1$ the material is fully broken.

2.1. Phase field approximation of crack

The scalar phase field $d(\mathbf{x}, t)$ can be determined through solving the following boundary value problem subjected to Dirichlet boundary conditions $d = 1$ on the crack (see [39] for more details):

$$\begin{cases} d(\mathbf{x}, t) - \ell^2 \Delta d(\mathbf{x}, t) = 0 \text{ in } \Omega, \\ d(\mathbf{x}, t) = 1 \text{ on } \Gamma, \\ \nabla d(\mathbf{x}, t) \cdot \mathbf{n} = 0 \text{ on } \partial\Omega, \end{cases} \quad (1)$$

where $\Delta(\cdot)$ and $\nabla(\cdot)$ are the Laplacian and gradient operator respectively, ℓ is a length scale parameter that governs the width of the regularization zone and gives for $\ell \rightarrow 0$ the exact sharp crack in Fig. 1(a), and \mathbf{n} the outward normal on $\partial\Omega$. It can be shown that (1) is the Euler-Lagrange equation associated with the variational problem:

$$d = \text{Arg} \left\{ \inf_{d \in S_d} \Gamma^d(d) \right\}, \quad \Gamma^d(d) = \int_{\Omega} \gamma_d(d) d\Omega, \quad S_d = \{d \mid d(\mathbf{x}) = 1, \forall \mathbf{x} \in \Gamma\}, \quad (2)$$

where $\Gamma^d(d)$ represents the total length of the crack in 2D and the total crack surface area in 3D, and $\gamma_d(d)$ is the crack surface density function per unit volume defined by:

$$\gamma_d(d) = \frac{d^2}{2\ell} + \frac{\ell}{2} \nabla d \cdot \nabla d, \quad (3)$$

where the second term in $\gamma_d(d)$ penalizes high values of $\nabla d(\mathbf{x})$ and where d varies between 0 and 1. Note that in the absence of the second right-hand term in (3), a local damage model is found, with well-known related non-convergence issues with respect to the mesh discretization.

It must be noted that, ℓ does not represent physically the exact crack width, but a parameter which is used to regularize the discontinuities. It has been shown that this parameter can be treated as a material parameter related to the Young's modulus, the tensile strength, and the critical energy release rate of the material in [10, 48, 68]. In our previous work [47], an inverse approach was developed to identify this parameter, by combining simulations and experiments. More recently in [45], G. Molnár et al. assessed its mechanical significance with the help of the coupled criterion.

2.2. Variational framework

We follow the framework presented in [2] to construct the variational principle, which involves: irreversibility condition, stability condition and energy balance. In this framework, stability condition provides mechanical balance equation and damage criteria. The energy balance provides damage consistency. The total energy for a cracked body is defined as

$$W(\mathbf{u}, d) = \int_{\Omega} \psi_e(\boldsymbol{\varepsilon}(\mathbf{u}), d) d\Omega + \int_{\Omega} \psi_d(d) d\Omega - \int_{\partial\Omega_F} \mathbf{F} \cdot \mathbf{u} dS - \int_{\Omega} \mathbf{f} \cdot \mathbf{u} d\Omega, \quad (4)$$

in which \mathbf{u} is displacement field, $\boldsymbol{\varepsilon}(\mathbf{u}) = \frac{1}{2}(\nabla\mathbf{u} + \nabla\mathbf{u}^T)$, \mathbf{f} and \mathbf{F} are body forces and prescribed traction over the boundary $\partial\Omega_F$, respectively. Above, ψ_d is the damage dissipative potential defined as

$$\psi_d = g_c \gamma_d(d), \quad (5)$$

where $\gamma_d(d)$ is defined in (3), and g_c is the Griffith-type critical energy release rate. ψ_e is the stored elastic energy density function defined as [39]

$$\psi_e(\boldsymbol{\varepsilon}, d) = \left((1-d)^2 + k \right) \psi_e^+(\boldsymbol{\varepsilon}) + \psi_e^-(\boldsymbol{\varepsilon}) \quad (6)$$

in which k is a small numerical parameter to prevent loss of definite posedness of the elastic tensor in case of full damage, ψ_e^+ and ψ_e^- are the tensile and compressive energies,

$$\psi_e^{\pm} = \frac{1}{2} \lambda \langle \text{tr}[\boldsymbol{\varepsilon}] \rangle_{\pm}^2 + \mu \text{tr}[\boldsymbol{\varepsilon}^{\pm}]^2, \quad (7)$$

with λ and μ the standard lame parameters. Note that only tensile damage degradation is taken into account in the elastic energy density (6) through a decomposition of the elastic strain $\boldsymbol{\varepsilon}$ into tensile/positive and compressive/negative parts:

$$\boldsymbol{\varepsilon} = \boldsymbol{\varepsilon}^+ + \boldsymbol{\varepsilon}^- \quad \text{with} \quad \boldsymbol{\varepsilon}^{\pm} = \sum_{i=1}^3 \langle \varepsilon^i \rangle_{\pm} \mathbf{n}^i \otimes \mathbf{n}^i, \quad (8)$$

where $\langle x \rangle_{\pm} = \frac{1}{2}(x \pm |x|)$, ε^i and \mathbf{n}^i are the eigenvalues and eigenvectors of $\boldsymbol{\varepsilon}$.

2.2.1. Irreversibility condition

The irreversibility condition is imposed on the damage variable to avoid material regeneration. It can be expressed as

$$\dot{d} \geq 0, \quad 0 \leq d \leq 1 \quad (9)$$

which is ensured by using an appropriate history function [39].

2.2.2. First-order stability condition

The first order stability condition (see [43, 44, 51]) is expressed by:

$$D_{\delta \mathbf{u}} W(\mathbf{u}, d) + D_{\delta d} W(\mathbf{u}, d) \geq 0, \quad (10)$$

where

$$D_{\mathbf{v}} f(\mathbf{u}) = \left[\frac{d}{dh} f(\mathbf{u} + h\mathbf{v}) \right]_{h=0}. \quad (11)$$

is the directional derivative. Applied to (4), it yields:

$$\int_{\Omega} \boldsymbol{\sigma} : \boldsymbol{\varepsilon}(\delta \mathbf{u}) d\Omega + \int_{\Omega} \left(\frac{\partial \psi_e}{\partial d} + \frac{\partial \psi_d}{\partial d} \right) \delta d d\Omega - \int_{\partial \Omega_F} \mathbf{F} \cdot \delta \mathbf{u} dS - \int_{\Omega} \mathbf{f} \cdot \delta \mathbf{u} d\Omega \geq 0 \quad (12)$$

where

$$\boldsymbol{\sigma} = \frac{\partial \psi_e}{\partial \boldsymbol{\varepsilon}} = \left((1-d)^2 + k \right) (\lambda \langle \text{tr} [\boldsymbol{\varepsilon}] \rangle_+ \mathbf{1} + 2\mu \boldsymbol{\varepsilon}^+) + \lambda \langle \text{tr} [\boldsymbol{\varepsilon}] \rangle_- \mathbf{1} + 2\mu \boldsymbol{\varepsilon}^- \quad (13)$$

in which $\mathbf{1}$ is the second-order identity tensor and $\boldsymbol{\sigma}^+/\boldsymbol{\sigma}^-$ are the undamaged tensile/compressive stress tensors.

From (12), the following results stem out:

- For $\delta d = 0$, find $\mathbf{u} \in \mathcal{S}_u$, $\mathcal{S}_u = \{ \mathbf{u} | \mathbf{u}(\mathbf{x}) = \bar{\mathbf{u}} \text{ on } \partial \Omega_u, \mathbf{u} \in H^1(\Omega) \}$ such that:

$$\int_{\Omega} \boldsymbol{\sigma} : \boldsymbol{\varepsilon}(\delta \mathbf{u}) d\Omega - \int_{\partial \Omega_F} \mathbf{F} \cdot \delta \mathbf{u} dS - \int_{\Omega} \mathbf{f} \cdot \delta \mathbf{u} d\Omega = 0, \quad (14)$$

which is the weak form of the mechanical equilibrium equation, with $\delta \mathbf{u} \in \mathcal{S}_u^0$, $\mathcal{S}_u^0 = \{ \delta \mathbf{u} | \delta \mathbf{u}(\mathbf{x}) = 0 \text{ on } \partial \Omega_u, \mathbf{u} \in H^1(\Omega) \}$.

- For $\delta \mathbf{u} = \mathbf{0}$ we obtain:

$$\int_{\Omega} \left(\frac{\partial \psi_e}{\partial d} + \frac{\partial \psi_d}{\partial d} \right) \delta d d\Omega \geq 0 \quad (15)$$

which is the weak form of the damage criterion. In local form, it can be expressed as:

$$f^d(d) = - \left(\frac{\partial \psi_e}{\partial d} + \frac{\partial \psi_d}{\partial d} \right) \leq 0 \text{ in } \Omega. \quad (16)$$

2.2.3. Energy balance

The energy balance represents the need for the total energy to remain constant as the state variables evolve. Following a procedure analogous to the treatment of the stability condition, this condition leads to

$$\int_{\Omega} \left[-\boldsymbol{\sigma} : \boldsymbol{\varepsilon}(\dot{\mathbf{u}}) - \left(\frac{\partial \psi_e}{\partial d} + \frac{\partial \psi_d}{\partial d} \right) \dot{d} \right] d\Omega + \int_{\partial \Omega_F} \mathbf{F} \cdot \dot{\mathbf{u}} dS + \int_{\Omega} \mathbf{f} \cdot \dot{\mathbf{u}} d\Omega = 0. \quad (17)$$

For $\dot{\mathbf{u}} = \mathbf{0}$, and using (16), the damage consistency condition is obtained:

$$f^d(d) \dot{d} = 0. \quad (18)$$

2.2.4. Alternate minimization

In this section, a staggered alternate minimization algorithm is applied, which naturally stems out from the energetic principles. This procedure takes advantage of the fact that although the global energy is non-convex, it is convex with respect to \mathbf{u} and d individually [1, 37]. With the total energy (4) at hand, the alternate minimization follows.

- Minimization with respect to the displacement field:

$$D_{\delta \mathbf{u}} W(\mathbf{u}, d) = 0 \quad (19)$$

which leads to

$$R_1 = \int_{\Omega} \boldsymbol{\sigma} : \boldsymbol{\varepsilon}(\delta \mathbf{u}) d\Omega - \int_{\partial \Omega_F} \mathbf{F} \cdot \delta \mathbf{u} dS - \int_{\Omega} \mathbf{f} \cdot \delta \mathbf{u} d\Omega = 0 \quad (20)$$

which corresponds to the weak form of the mechanical problem to be solved for \mathbf{u} , given d .

- Minimization with respect to the damage field:

$$D_{\delta d} W(\mathbf{u}, d) = \int_{\Omega} \left(\frac{\partial \psi_e}{\partial d} + \frac{\partial \psi_d}{\partial d} \right) \delta d d\Omega = 0. \quad (21)$$

which corresponds to the global problem to be solved to find the field $d(\mathbf{x})$ (phase field problem), given \mathbf{u} .

2.2.5. Governing equations

The associated Euler-Lagrange equations to (20) are given by:

$$\left\{ \begin{array}{l} \nabla \cdot \boldsymbol{\sigma} + \mathbf{f} = \mathbf{0} \text{ in } \Omega, \\ \mathbf{u} = \bar{\mathbf{u}} \text{ on } \partial \Omega_u, \\ \boldsymbol{\sigma} \mathbf{n} = \mathbf{F} \text{ on } \partial \Omega_F. \end{array} \right. \quad (22)$$

Using (21) and the property:

$$(\Delta d) \delta d = \nabla \cdot (\nabla d \delta d) - \nabla d \cdot \nabla(\delta d) \quad (23)$$

as well as the divergence theorem and $\nabla d \cdot \mathbf{n} = 0$, we obtain the weak form of the phase field problem as:

$$\int_{\Omega} \left(\left\{ -2(1-d)\psi_e^+ + \frac{g_c d}{\ell} \right\} \delta d + g_c \ell \nabla d \cdot \nabla(\delta d) \right) d\Omega = 0. \quad (24)$$

To prescribe irreversibility, we employ the technique introduced in [41] which consists in substituting the above weak form with:

$$\int_{\Omega} (\{-2(1-d)\mathcal{H}(\varepsilon) + 2\psi_c d\} \delta d + 2\psi_c \ell^2 \nabla d \cdot \nabla(\delta d)) d\Omega = 0, \quad (25)$$

Table 1: Governing equations of the phase field model.

Irreversibility	$\dot{d} \geq 0, \quad 0 \leq d \leq 1$
Mechanical balance	$\nabla \cdot \boldsymbol{\sigma} + \mathbf{f} = 0$ in Ω $\mathbf{u} = \bar{\mathbf{u}}$ on $\partial\Omega_u, \quad \boldsymbol{\sigma} \mathbf{n} = \mathbf{F}$ on $\partial\Omega_F$
Constitutive law	$\boldsymbol{\sigma} = \left((1-d)^2 + k \right) \left(\lambda \langle \text{tr} [\boldsymbol{\varepsilon}] \rangle_+ \mathbf{1} + 2\mu \boldsymbol{\varepsilon}^+ \right) + \lambda \langle \text{tr} [\boldsymbol{\varepsilon}] \rangle_- \mathbf{1} + 2\mu \boldsymbol{\varepsilon}^-$
Damage criterion	$\psi_c (d - \ell^2 \Delta d) - (1-d) \mathcal{H}(\boldsymbol{\varepsilon}) \geq 0$ $\mathcal{H}(\boldsymbol{\varepsilon}) = \max_{s \in [0, t]} \left[\langle \psi_e^+(\boldsymbol{\varepsilon}, s) - \psi_c \rangle_+ \right]$
Damage consistency	$(\psi_c (d - \ell^2 \Delta d) - (1-d) \mathcal{H}(\boldsymbol{\varepsilon})) \dot{d} = 0$

in which

$$\mathcal{H}(\boldsymbol{\varepsilon}) = \max_{s \in [0, t]} \left[\langle \psi_e^+(\boldsymbol{\varepsilon}, s) - \psi_c \rangle_+ \right] \quad (26)$$

and ψ_c is a specific fracture energy density, which can be further related to a critical fracture stress σ_c by:

$$\psi_c = \frac{1}{2E} \sigma_c^2, \quad (27)$$

where E is the Young's modulus.

The corresponding Euler-Lagrange equations to (25) are given by:

$$\left\{ \begin{array}{l} \psi_c (d - \ell^2 \Delta d) = (1-d) \mathcal{H}(\boldsymbol{\varepsilon}) \\ \nabla d \cdot \mathbf{n} = 0 \quad \text{on } \partial\Omega, \\ d = 1 \quad \text{on } \Gamma. \end{array} \right. \quad (28)$$

The different equations of the model are summarized in Table 1. The FEM discretization details are provided in Appendix.

3. SIMP Topology optimization formulation

In this section, we present a SIMP topology optimization framework for maximizing the fracture resistance of a two-phase (composite) structure.

3.1. Optimization problem statement

The topology optimization problem is conducted with respect to a density variable $\rho(\mathbf{x})$ which is associated with the inclusion phase. In other words, $\rho(\mathbf{x}) = 1$ corresponds to inclusion phase and $\rho(\mathbf{x}) = 0$ corresponds to the matrix phase.

For stability considerations, here displacement-controlled loading is adopted. For a prescribed displacement load, the fracture resistance maximization is equivalent to the maximization of the

mechanical work. Recalling that the fracture problem is quasi-static, we introduce a pseudo time t associated with the external load evolution, with $t \in [0, t^{max}]$, where t^{max} denotes the maximum loading time corresponding to the maximum prescribed displacement \bar{u}^{max} at the failure step.

The optimization problem is then defined as follows:

$$\text{Maximize : } J(\rho, \mathbf{u}, d) \quad (29)$$

$$\text{subject : } R_1(\rho, \mathbf{u}(t), d(t)) = 0, \quad \forall t \in [0, t^{max}] \quad (30)$$

$$R_2(\rho, \mathbf{u}(t), d(t)) = 0, \quad \forall t \in [0, t^{max}] \quad (31)$$

$$f^{inc} = \frac{V(\Omega^{inc})}{V(\Omega)} = \frac{\int_{\Omega} \rho(\mathbf{x}) d\Omega}{V(\Omega)} \quad (32)$$

$$0 \leq \rho(\mathbf{x}) \leq 1 \quad (33)$$

$$\mathbf{u}(t) \in \mathcal{S}_u \quad (34)$$

$$d(t) \in \mathcal{S}_d, \quad (35)$$

where $V(\Omega^{inc})$ is the inclusion volume, $V(\Omega)$ is the total volume of the domain, and

$$J = \int_0^{t^{max}} \mathbf{F}_{ext}(t) \cdot \bar{\mathbf{u}}(t) dt, \quad (36)$$

where R_1 and R_2 are given by (20) and (59), \mathbf{F}_{ext} is the external force response at the load point and f^{inc} is the prescribed volume fraction of the inclusion phase.

Following [15], the material interpolations for the two-phase material are defined as

$$\begin{cases} E(\mathbf{x}) = (\rho(\mathbf{x}))^p E_{inc} + (1 - (\rho(\mathbf{x}))^p) E_{mat}, \\ \psi_c(\mathbf{x}) = (\rho(\mathbf{x}))^p \psi_{c,inc} + (1 - (\rho(\mathbf{x}))^p) \psi_{c,mat}, \end{cases} \quad (37)$$

where E and ψ_c are the Young's modulus and the fracture energy density. $(\cdot)_{inc}$ and $(\cdot)_{mat}$ are the parameters corresponding to the inclusion and the matrix phase, respectively. The Poisson's ratios of the two material phases are assumed identical. Above, p is the penalty coefficient to enforce solutions close to $\rho = 0$ or 1. Following [58], we choose $p = 3$. Fig. 2 shows the difference of Young's modulus interpolation for SIMP and BESO [66]. The continuous material interpolations for SIMP ensures that the optimization problem is smooth and that the objective function is differentiable.

3.2. Discrete topology optimization problem

The design domain Ω is discretized into N_e finite elements and each element e is assigned with a topology design variable, or element density ρ_e , which is allowed to vary continuously in the range $[0, 1]$. Here, a density of $\rho_e = 1$ corresponds to an element completely filled with the inclusion phase, whereas $\rho_e = 0$ corresponds to an element completely filled with the matrix phase. We define the vector $\{\boldsymbol{\rho}\} = \{\rho_1, \rho_2, \dots, \rho_{N_e}\}$ containing the discrete values of densities in elements of the mesh.

The discrete form of (29)-(35) is then defined as:

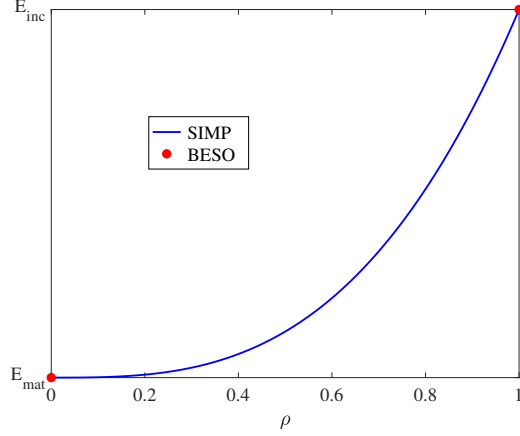


Figure 2: Young's modulus interpolations for SIMP and BESO.

$$\text{Maximize : } J^{\Delta u}(\boldsymbol{\rho}, \mathbf{u}, \mathbf{d}) \quad (38)$$

$$\text{subject : } \mathbf{K}_u^n \mathbf{u}^n - \mathbf{F}_u^n = \mathbf{0}, \quad n = 1, 2, \dots, n_{load} \quad (39)$$

$$\sum_{e=1}^{N_e} \rho_e v_e / \left(\sum_{e=1}^{N_e} v_e \right) = f^{inc} \quad (40)$$

$$0 \leq \rho_e \leq 1, \quad e = 1, 2, \dots, N_e \quad (41)$$

$$\mathbf{u}^n \in \mathcal{S}_u, \quad n = 1, 2, \dots, n_{load} \quad (42)$$

$$\mathbf{d}^n \in \mathcal{S}_d, \quad n = 1, 2, \dots, n_{load}, \quad (43)$$

and $J^{\Delta u}$ in (38) is approximated by:

$$J^{\Delta u} = \sum_{n=1}^{n_{load}} \Delta J^n \approx \frac{1}{2} \sum_{n=1}^{n_{load}} (\mathbf{F}_{ext}^n + \mathbf{F}_{ext}^{n-1})^T \Delta \mathbf{u}^n, \quad (44)$$

where $\Delta \mathbf{u}^n$ denotes the prescribed load increment at load n . Above, v_e is the volume (area in 2D) of the e -th element and f^{inc} is the target inclusion volume which is prescribed during the optimization process. The stiffness matrix \mathbf{K}_u^n at the n -th load increment is constructed following (67).

It should be noted that in this work the continuous topology design variable $\rho_e \in [0, 1]$ allows using well-proven gradient-based optimization update approaches (e.g., Optimality Criteria methods (OC) [11, 58], the Method of Moving Asymptotes (MMA) [60] and so on), in turn ensuring algorithmic convergence within a reasonable number of topological iterations (from 10 to 1000 iterations) [59].

Another important remark is that in the present paper, we do not explicitly use the second constraint (31) in the discrete problem (38)-(43) and in the following sensitivity analysis. In fact, this constraint is taken into account implicitly as the regularized fracture problem is solved in a staggered solving procedure. When the mechanical problem (20) is solved, the damage variable

$d(\mathbf{x})$ is assumed to be known from previous iteration and then the phase field problem equation R_2 in (59) is supposed to be verified. This assumption considerably simplifies the sensitivity analysis presented next.

3.3. Sensitivity analysis

In order to solve the optimization problem (38)-(43), the sensitivity of the objective function J corresponding to change in the design variable must be determined. The derivation of the sensitivity requires using the adjoint method (e.g., [18, 66]). Assuming that the mechanical problem (65) has been solved, we introduce the Lagrangian:

$$J^{\Delta u} \approx \bar{J} = \frac{1}{2} \sum_{n=1}^{n_{load}} \left\{ (\mathbf{F}_u^n + \mathbf{F}_u^{n-1})^T \Delta \mathbf{u}^n + (\boldsymbol{\lambda}_1^n)^T \mathbf{R}^n + (\boldsymbol{\lambda}_2^n)^T \mathbf{R}^{n-1} \right\} \quad (45)$$

in which \mathbf{R}^n and \mathbf{R}^{n-1} are the residuals of (65) at n -th and $(n-1)$ -th load increments, respectively. $\boldsymbol{\lambda}_1^n$ and $\boldsymbol{\lambda}_2^n$ are Lagrange multipliers which have the same dimension with the displacement vector \mathbf{u} .

Notice that for displacement-controlled loading problem, displacement components at the boundary nodes and force components at the free nodes are fixed, hence, they are independent of the current value of ρ . Here we introduce a division of all degrees of freedom into essential (index E; associated with Dirichlet boundary conditions) and free (index F) nodal values. For a vector \mathbf{v} and a matrix \mathbf{M} we have

$$\mathbf{v} \sim \begin{bmatrix} \mathbf{v}_E \\ \mathbf{v}_F \end{bmatrix} \quad \text{and} \quad \mathbf{M} \sim \begin{bmatrix} \mathbf{M}_{EE} & \mathbf{M}_{EF} \\ \mathbf{M}_{FE} & \mathbf{M}_{FF} \end{bmatrix}. \quad (46)$$

We then have these unknowns at the n -th load increment

$$\frac{\partial \mathbf{u}^n}{\partial \rho_e} = \begin{bmatrix} \mathbf{0} \\ \frac{\partial \mathbf{u}_F^n}{\partial \rho_e} \end{bmatrix}, \quad \frac{\partial \Delta \mathbf{u}^n}{\partial \rho_e} = \begin{bmatrix} \mathbf{0} \\ \frac{\partial \Delta \mathbf{u}_F^n}{\partial \rho_e} \end{bmatrix}, \quad \mathbf{F}_u^n = \begin{bmatrix} \mathbf{F}_{u,E}^n \\ \mathbf{0} \end{bmatrix}, \quad \frac{\partial \mathbf{F}_u^n}{\partial \rho_e} = \begin{bmatrix} \frac{\partial \mathbf{F}_{u,E}^n}{\partial \rho_e} \\ \mathbf{0} \end{bmatrix} \quad (47)$$

Here for arbitrary load increment indices $n = 1, \dots, n_{load}$, $m = 1, \dots, n_{load}$, we have

$$\frac{\partial}{\partial \rho_e} \left((\mathbf{F}_u^m)^T \Delta \mathbf{u}^n \right) = \left(\frac{\partial \mathbf{F}_u^m}{\partial \rho_e} \right)^T \Delta \mathbf{u}^n + (\mathbf{F}_u^m)^T \frac{\partial \Delta \mathbf{u}^n}{\partial \rho_e} = \left(\frac{\partial \mathbf{F}_u^m}{\partial \rho_e} \right)^T \Delta \mathbf{u}^n. \quad (48)$$

With the above property at hand, the derivative of the objective function J in (45) is given by

$$\frac{\partial \bar{J}}{\partial \rho_e} = \frac{1}{2} \sum_{n=1}^{n_{load}} \left\{ \frac{\partial (\mathbf{F}_u^n + \mathbf{F}_u^{n-1})^T}{\partial \rho_e} \Delta \mathbf{u}^n + (\boldsymbol{\lambda}_1^n)^T \frac{\partial \mathbf{R}^n}{\partial \rho_e} + (\boldsymbol{\lambda}_2^n)^T \frac{\partial \mathbf{R}^{n-1}}{\partial \rho_e} \right\}. \quad (49)$$

The derivatives of \mathbf{R}^m at the equilibrium of the m -th load increment with respect to ρ_e can be expanded as

$$\frac{\partial \mathbf{R}^m}{\partial \rho_e} = \frac{\partial \mathbf{F}_u^m}{\partial \rho_e} - \frac{\partial \mathbf{K}_u^m}{\partial \rho_e} \mathbf{u}^m - \mathbf{K}_u^m \frac{\partial \mathbf{u}^m}{\partial \rho_e}. \quad (50)$$

Using (47) and (50), (49) can be reformulated as

$$\begin{aligned} \frac{\partial \bar{J}}{\partial \rho_e} = & \frac{1}{2} \sum_{n=1}^{n_{load}} \left\{ \left(\frac{\partial \mathbf{F}_{u,E}^n}{\partial \rho_e} \right)^T (\Delta \mathbf{u}_E^n + \boldsymbol{\lambda}_{1,E}^n) + \left(\frac{\partial \mathbf{F}_{u,E}^{n-1}}{\partial \rho_e} \right)^T (\Delta \mathbf{u}_E^n + \boldsymbol{\lambda}_{2,E}^n) \right. \\ & \left. - (\boldsymbol{\lambda}_1^n)^T \left(\frac{\partial \mathbf{K}_u^n}{\partial \rho_e} \mathbf{u}^n + \mathbf{K}_u^n \frac{\partial \mathbf{u}^n}{\partial \rho_e} \right) - (\boldsymbol{\lambda}_2^n)^T \left(\frac{\partial \mathbf{K}_u^{n-1}}{\partial \rho_e} \mathbf{u}^{n-1} + \mathbf{K}_u^{n-1} \frac{\partial \mathbf{u}^{n-1}}{\partial \rho_e} \right) \right\}. \end{aligned} \quad (51)$$

In order to eliminate the unknowns $\frac{\partial \mathbf{F}_{u,E}^n}{\partial \rho_e}$ and $\frac{\partial \mathbf{F}_{u,E}^{n-1}}{\partial \rho_e}$ in (51), we choose

$$\boldsymbol{\lambda}_{1,E}^n = -\Delta \mathbf{u}_E^n \quad \text{and} \quad \boldsymbol{\lambda}_{2,E}^n = -\Delta \mathbf{u}_E^n. \quad (52)$$

Then we can re-write (51) as

$$\begin{aligned} \frac{\partial \bar{J}}{\partial \rho_e} = & -\frac{1}{2} \sum_{n=1}^{n_{load}} \left\{ (\boldsymbol{\lambda}_1^n)^T \frac{\partial \mathbf{K}_u^n}{\partial \rho_e} \mathbf{u}^n + (\mathbf{K}_{u,FE}^n \boldsymbol{\lambda}_{1,E}^n + \mathbf{K}_{u,FF}^n \boldsymbol{\lambda}_{1,F}^n)^T \frac{\partial \mathbf{u}_F^n}{\partial \rho_e} \right. \\ & \left. + (\boldsymbol{\lambda}_2^n)^T \frac{\partial \mathbf{K}_u^{n-1}}{\partial \rho_e} \mathbf{u}^{n-1} + (\mathbf{K}_{u,FE}^{n-1} \boldsymbol{\lambda}_{2,E}^n + \mathbf{K}_{u,FF}^{n-1} \boldsymbol{\lambda}_{2,F}^n)^T \frac{\partial \mathbf{u}_F^{n-1}}{\partial \rho_e} \right\}. \end{aligned} \quad (53)$$

To eliminate the unknowns $\frac{\partial \mathbf{u}_F^n}{\partial \rho_e}$ and $\frac{\partial \mathbf{u}_F^{n-1}}{\partial \rho_e}$ in (53), we choose

$$\boldsymbol{\lambda}_{1,F}^n = (\mathbf{K}_{u,FF}^n)^{-1} \mathbf{K}_{u,FE}^n \Delta \mathbf{u}_E^n \quad \text{and} \quad \boldsymbol{\lambda}_{2,F}^n = (\mathbf{K}_{u,FF}^{n-1})^{-1} \mathbf{K}_{u,FE}^{n-1} \Delta \mathbf{u}_E^n. \quad (54)$$

Using (52) and (54), we can obtain the final objective derivative

$$\frac{\partial \bar{J}}{\partial \rho_e} = -\frac{1}{2} \sum_{n=1}^{n_{load}} \left\{ (\boldsymbol{\lambda}_1^n)^T \frac{\partial \mathbf{K}_u^n}{\partial \rho_e} \mathbf{u}^n + (\boldsymbol{\lambda}_2^n)^T \frac{\partial \mathbf{K}_u^{n-1}}{\partial \rho_e} \mathbf{u}^{n-1} \right\}. \quad (55)$$

For each element e , (55) can be re-written as

$$\begin{aligned} \alpha_e &= \sum_{n=1}^{n_{load}} (\Delta \alpha_e)^n \\ &= -\frac{1}{2} \sum_{n=1}^{n_{load}} \left\{ (\boldsymbol{\lambda}_{1,e}^n)^T \frac{\partial \mathbf{k}_{u,e}^n}{\partial \rho_e} \mathbf{u}_e^n + (\boldsymbol{\lambda}_{2,e}^n)^T \frac{\partial \mathbf{k}_{u,e}^{n-1}}{\partial \rho_e} \mathbf{u}_e^{n-1} \right\}, e = 1, \dots, N_e, \end{aligned} \quad (56)$$

in which $(\cdot)_e$ is the element component of (\cdot) and $\mathbf{k}_{u,e}^n$ is the element stiffness matrix for element e at the n -th load step. For the sake of simplicity, we use α_e and $\boldsymbol{\alpha}$ to represent element sensitivity and vector of all element sensitivities. It should be noted that in this work we need to evaluate the sensitivities of all elements, unlike our previous works [21, 66] which only compute the sensitivities of the inclusion elements and set directly the sensitivities of the matrix elements to zeros. It is worth noting that the present framework can easily include interfacial damage by using the extended phase field framework proposed in [50]. Such an extension in the context of BESO can be found in [20, 21]. Such formulation allows using a fixed regular mesh, which is advantageous for TO algorithms. In contrast, other formulation have been proposed to include interfacial damage within Phase Field by using cohesive elements e.g. in [24, 25], but require meshing explicitly the interfaces. This might not be well suited to TO problems, where 3D complex inclusion geometries can be involved, as shown in the next examples.

4. Overall algorithm

This section presents the overall algorithms of the proposed method. We first introduce the algorithm used to simulate one crack simulation from the initial nucleation to complete failure, which will be used within one step of the topology optimization. During this simulation, the sensitivities are computed at the same time as the fracture evolution. Then, the overall topology optimization is presented.

In the fracture evolution problem, a staggered scheme is employed following [39], where at each load increment the crack phase field problem is solved for fixed displacement field which is known from the previous time step. The displacement problem is then solved for the obtained crack phase field. Finally the sensitivity analysis is implemented after the staggered scheme.

The flowchart for fracture evolution problem and sensitivity calculations is provided in Algorithm 1.

Algorithm 1: Fracture evolution problem and sensitivity calculations.

Input: Densities $\{\rho^k\}$
Output: the total mechanical work J^k and sensitivity vector α^k
Initialize $\mathbf{u}^0 = \mathbf{0}$, $\mathcal{H}^0 = \mathbf{0}$, $J^0 = 0$ and $\alpha^0 = \mathbf{0}$.
Loop over load increments n_{load}
for $n = 1, \dots, n_{load}$ **do**
 %% Crack phase field problem %%
 Given \mathbf{u}^{n-1} and \mathcal{H}^{n-1} ,
 Compute \mathcal{H}^n by (26)
 Compute \mathbf{K}_d^n and \mathbf{F}_d^n from (62) and (63)
 Compute the crack phase field \mathbf{d}^n from (61)
 %% Displacement problem %%
 Given \bar{u}^n and \mathbf{d}^n
 Compute \mathbf{K}_u^n and \mathbf{F}_u^n from (67) and (66)
 Compute the displacement field \mathbf{u}^n from (65)
 %% Sensitivity calculations %%
 Compute Lagrange multipliers λ_1^n and λ_2^n from (52) and (54)
 Compute increment of sensitivity vector $\Delta\alpha^n$ with λ_1^n and λ_2^n from (56)
 Compute increment of mechanical work ΔJ^n from (44)
 Update $\alpha^n = \alpha^{n-1} + \Delta\alpha^n$ and $J^n = J^{n-1} + \Delta J^n$
 $n = n + 1$
end
 $\alpha^k = \alpha^{n_{load}}$ and $J^k = J^{n_{load}}$

In order to remove instabilities such as checkerboard patterns and to avoid mesh-dependency in topology optimization process, element sensitivities are smoothed by means of a filtering scheme [58]

$$\alpha_e = \frac{\sum_{j=1}^{N_e} w_{ej} \alpha_j}{\sum_{j=1}^{N_e} w_{ej}}, \quad (57)$$

in which w_{ej} is a linear weight factor

$$w_{ej} = \max(0, r_{min} - \Delta(e, j)) \quad (58)$$

which is determined by the prescribed filter radius r_{\min} and the element center-to-center distance $\Delta(e, j)$ between element e and j .

The optimization problem (29)-(35) could be solved using several different approaches such as OC method [11, 58] and the MMA [60] as illustrated in section 3.1. In this work, the OC method is employed to update the design variables. The overall algorithm is illustrated in Algorithm 2.

Algorithm 2: Overall topology optimization algorithm

```

Initialize inclusion densities  $\{\rho^1\}$ .
%% Topology optimization iteration %%
Set  $k = 1, Err = 1$  and iterative tolerance  $tol$ 
while  $Err > tol$  do
    %% Regularized fracture problem and sensitivity calculations %%
    Compute regularized fracture problem, obtain sensitivity vector  $\alpha^k$  and total
    mechanical work  $J^k$  with  $\rho^k(\mathbf{x})$  from Algorithm 1
    %% Filtering scheme %%
    Obtain the smoothed  $\alpha^k$  with (57)
    %% OC method %%
    Update the design variable  $\rho^{k+1}$  with smoothed  $\alpha^k$ 
    %% Compute convergence %%
    if  $k \geq 10$  then
        |  $Err = \frac{|\sum_{m=k-4}^k J^m - \sum_{n=k-9}^{k-5} J^n|}{\sum_{n=k-9}^{k-5} J^n}$ 
    else
        |  $Err = 1$ 
    end
     $k = k + 1$ 
end

```

5. Numerical examples

In this section we present several examples in both 2D and 3D to show the capability and convergence of the method, and compare the results with our previous work done by BESO method [66]. In all 2D examples uniform meshes of quadrilateral bilinear elements with the plane strain assumption have been employed. Uniform meshes of eight-node cubic elements have been used for the 3D examples. Both damage and displacement fields are discretized with the same finite element meshes. The characteristic length scale parameter ℓ for the phase field problem in (3) and the filter radius r_{\min} in (58) are both set to be twice the typical finite element size $\ell = r_{\min} = 2h_e$. For the sake of clear visualization, only the crack phase field with values higher than 0.4 in 2D examples and values higher than 0.95 in 3D examples are plotted. The material properties are shown in Table 2. The inclusion volume fraction f^{inc} is defined by (32). In the different simulations, the following features are noted.

- For SIMP topology optimization simulations, there is no initialization of the inclusion geometry. The initial density ρ_e^1 is set to be uniform and equal to f^{inc} .
- For BESO topology optimization simulations, an initial geometry of inclusion is required to match f^{inc} at the first iteration. If a homogeneous design is used, the volume fraction has

Table 2: Material parameters used in the numerical simulations [66]

Name	Notations	Inclusion	Matrix
Young's modulus	E^{inc}, E^{mat}	52 GPa	10.4 GPa
Poisson's ratio	ν	0.3	0.3
Critical fracture stress	$\sigma_c^{inc}, \sigma_c^{mat}$	0.03 GPa	0.01 GPa

to be reduced at each iteration by setting $\rho_e = 0$ in more elements, as ρ_e can only be zero or one in each element. We refer to this initial geometry to "initial BESO design".

- To evaluate the improvement of the fracture resistance in the present SIMP context which does not require an initial geometry, a "guess" design is defined in some examples to evaluate the improvement of the fracture resistance between optimized and guess designs.
- The volume fraction f^{inc} is fixed during the whole optimization process.
- To avoid interfering with the topology optimization process, a region around the initial crack is defined where the design variable are enforced to $\rho_e = 0$ (remain matrix material). This region is defined as embedding all nodes at a distance 2ℓ from the initial crack surface.
- The incremental loading process goes on until the reaction force is below a prescribed value, indicating that the structure is fully broken.

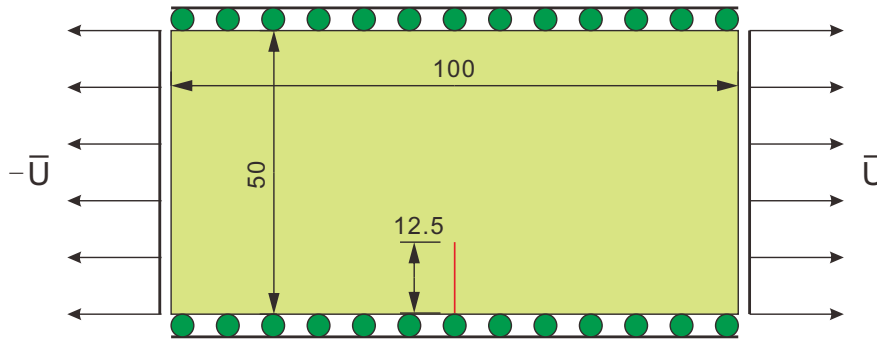


Figure 3: Plate with one pre-existing crack notch subjected to incremental traction load: geometry and boundary conditions.

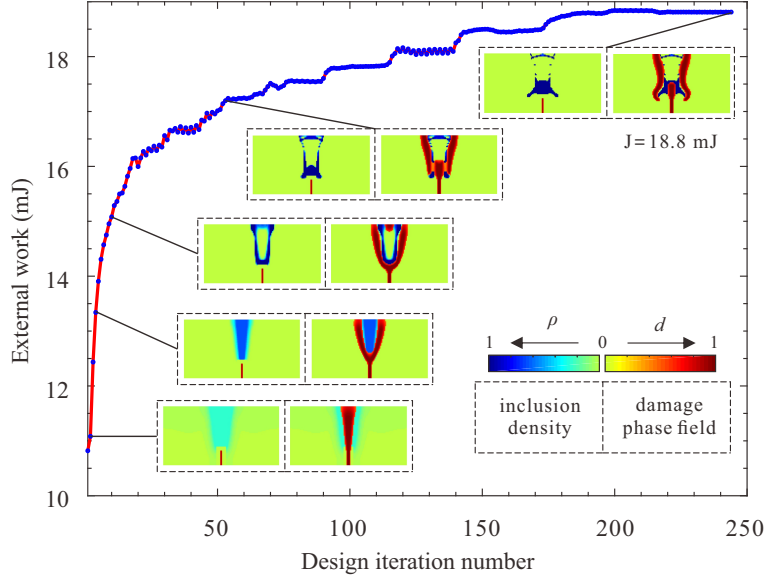


Figure 4: Evolution of inclusion topologies and associated final crack patterns ($f^{inc} = 5\%$).

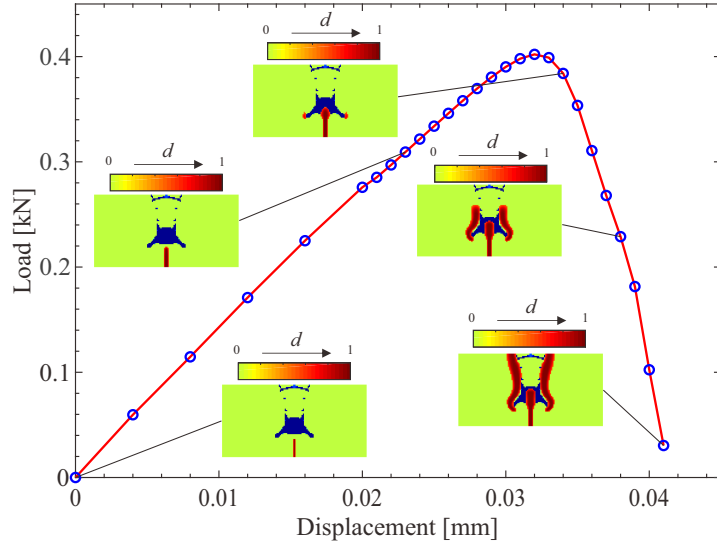


Figure 5: Load-displacement curve and crack propagation for the optimized design: (a) $\bar{U} = 0$ mm; (b) $\bar{U} = 0.023$ mm; (c) $\bar{U} = 0.034$ mm; (d) $\bar{U} = 0.038$ mm; (e) $\bar{U} = 0.041$ mm.

5.1. 2D reinforced plate with one pre-existing crack notch

In the following example, a 2D plate with one pre-existing crack notch, as described in Fig. 3, is considered. The structure is composed of a matrix material, and we seek the shape of an inclusion which provides the maximal fracture resistance for the whole composite structure. The dimensions of the plate are 100×50 mm², and the domain is uniformly discretized into 120×60 square bilinear elements. The boundary conditions are as follows: on the upper and lower ends,

the y -displacement are fixed, while the x -displacement are free. On the left and right ends, the horizontal displacements are prescribed with incremental displacement loads with $\Delta\bar{U} = 0.004$ mm for the first five load increments and $\Delta\bar{U} = 0.001$ mm for the following load increments. The pre-existing crack is simulated by prescribing Dirichlet conditions on the crack phase field with $d = 1$ along the crack. Additionally, the optimality convergence tolerance is set at 10^{-5} ($tol = 10^{-5}$).

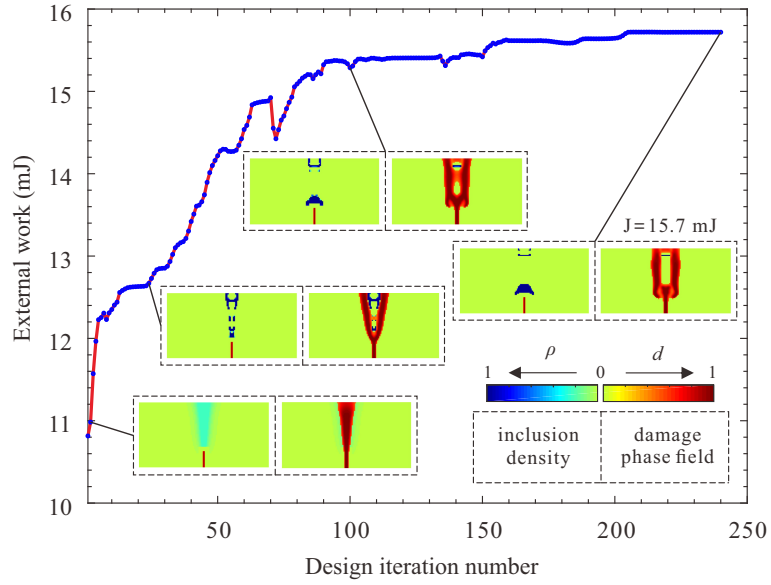


Figure 6: Evolution of inclusion topologies and associated final crack patterns ($f^{inc} = 2\%$).

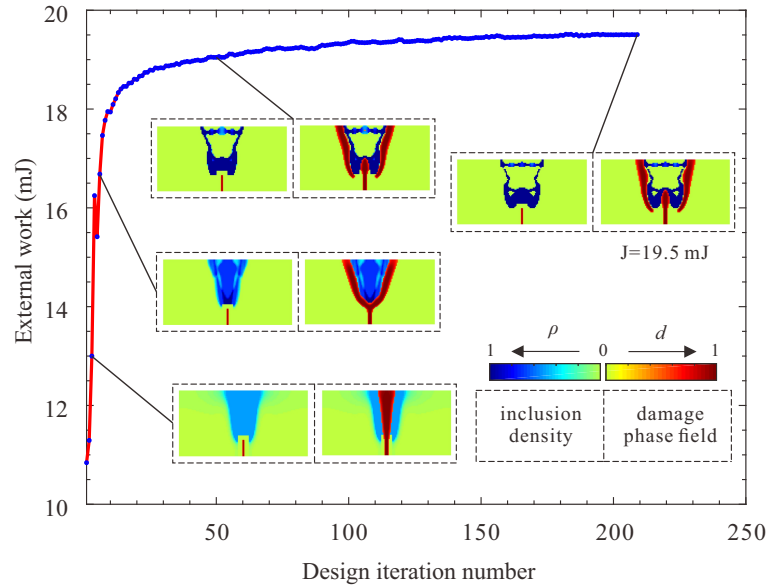


Figure 7: Evolution of inclusion topologies and associated final crack patterns ($f^{inc} = 10\%$).

Fig. 4 shows the evolution histories of inclusion topologies and their final crack patterns. Here, the inclusion volume fraction is set to $f^{inc} = 5\%$. As can be observed from Fig. 4, the fracture resistance of the composite structure increases with accumulation of the inclusion material around the crack paths obtained from previous design iteration and reduction of intermediate densities (sometimes called "grey zones" in the topology optimization studies), and then converges to an almost constant value of 18.8 mJ. Detailed propagation of the crack phase field corresponding to its load-displacement curve for the optimized design is shown in Fig. 5. The crack propagates vertically into the inclusion material and two other cracks initiate around the left and right corners of the inclusion pattern, and then continue to propagate until the structure is fully broken.

In order to illustrate the robustness of the method for other inclusion volume fractions and investigate the influence of f^{inc} on the numerical results, two additional simulations are conducted: $f^{inc} = 2\%$ and $f^{inc} = 10\%$. Fig. 6 and Fig. 7 show the evolution histories of inclusion topologies and their final crack patterns for cases $f^{inc} = 2\%$ and $f^{inc} = 10\%$, respectively. Fig. 8 shows comparison of the optimized designs and corresponding final crack patterns for cases $f^{inc} = 2\%$, $f^{inc} = 5\%$ and $f^{inc} = 10\%$. As can be observed, with the increase of the volume fraction, significant changes and more complex shapes of inclusions are obtained, in tandem with an increase of the fracture resistance.

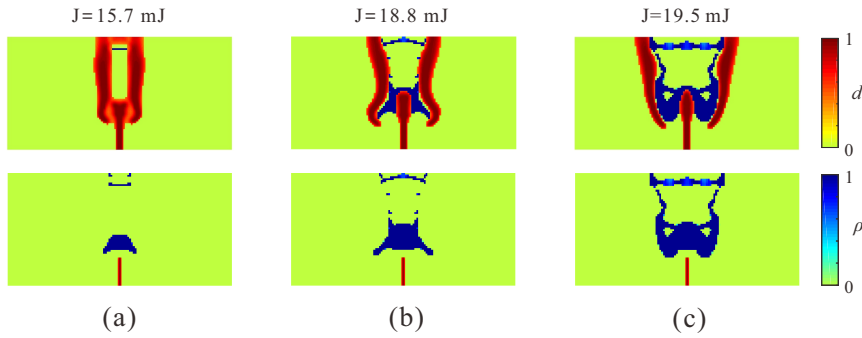


Figure 8: Comparison of optimized inclusion designs and corresponding final crack pattern at the failure load: (a) $f^{inc} = 2\%$, (b) $f^{inc} = 5\%$ and (c) $f^{inc} = 10\%$.

To investigate the effect of finite element mesh size on the numerical results, two additional simulations are performed for $f^{inc} = 5\%$ with finer meshes, involving 180×90 square bilinear elements, and 240×120 square bilinear elements, respectively. The filter radius r_{min} is fixed and is equal to 1.667 mm, and the length scale $\ell = 2h_e$ is changed with mesh refinement. Fig. 9 shows the comparison of optimized inclusion designs and corresponding final crack patterns for the three different mesh models. The corresponding load-displacement curves are shown in Fig. 10. From these two figures, it can be noticed that the optimized design changes with finer meshes, but the overall response of the structure as well as the optimized fracture energy does not change significantly. This suggests that simulations performed with reasonably fine meshes provide usable designs for practical applications. For this reason, in the following, we use the 120×60 mesh model.

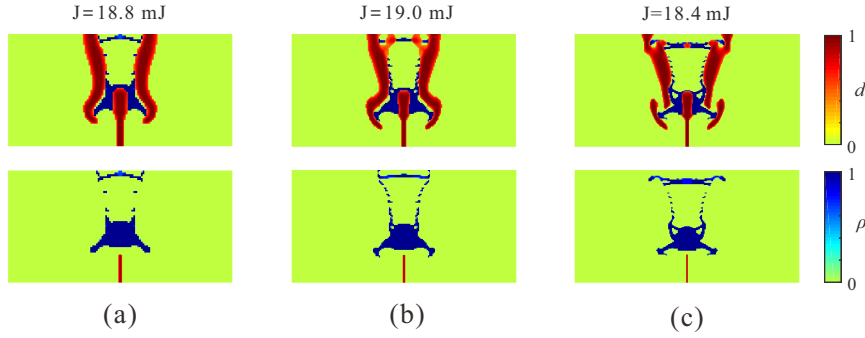


Figure 9: Comparison of optimized inclusion designs and corresponding final crack pattern for three different refined meshes: (a) 120×60 , (b) 180×90 and (c) 240×120 ($f^{inc} = 5\%$).

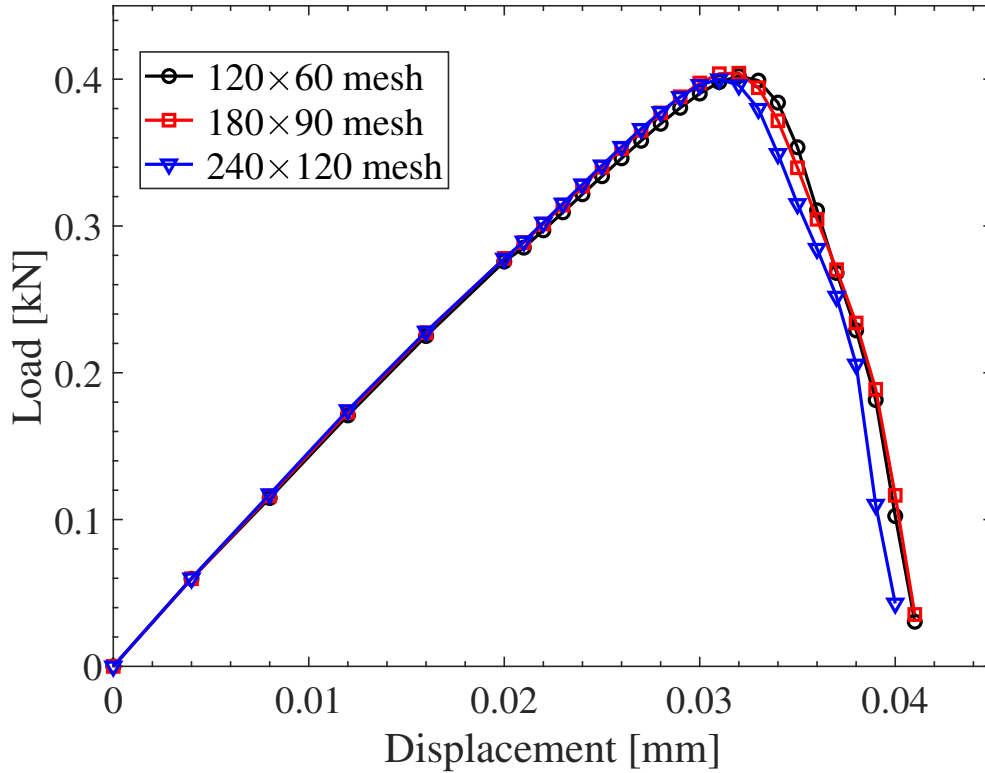


Figure 10: Load-displacement curves for different refined meshes ($f^{inc} = 5\%$).

In the following, we compare the proposed SIMP approach with BESO topology optimization solution [66]. Three additional simulations using the BESO method with the same volume fraction $f^{inc} = 5\%$ but different initial designs (see Fig. 11) are performed. To fully display the convergence histories of BESO method, we do not prescribe a convergence criterion for these three BESO simulations and let the algorithm run until a maximum number of iterations equal to 500 is reached. Fig. 12 shows the comparison of convergence histories for BESO and SIMP solutions. We can note

that in the case of BESO, the initial designs have a strong influence on the optimized objective function and on the convergence rate: (i) using BESO with design B, C or SIMP, the same convergence value 18.8 mJ is reached, while for initial design A with BESO the convergence value is about 19.6 mJ; (ii) solutions by BESO with initial designs B, C and SIMP solution require a similar number of convergence steps of about 200, while for initial design A with BESO the convergence number is about 400. From Fig. 12, we can also observe spurious oscillations for initial design A and C with BESO after a stable convergence value, while this does not seem to occur with SIMP. Fig. 11 shows the influence of initial design on the optimized design with BESO method. Fig. 13 shows the comparison of load-displacement curves for the 7 optimization processes.

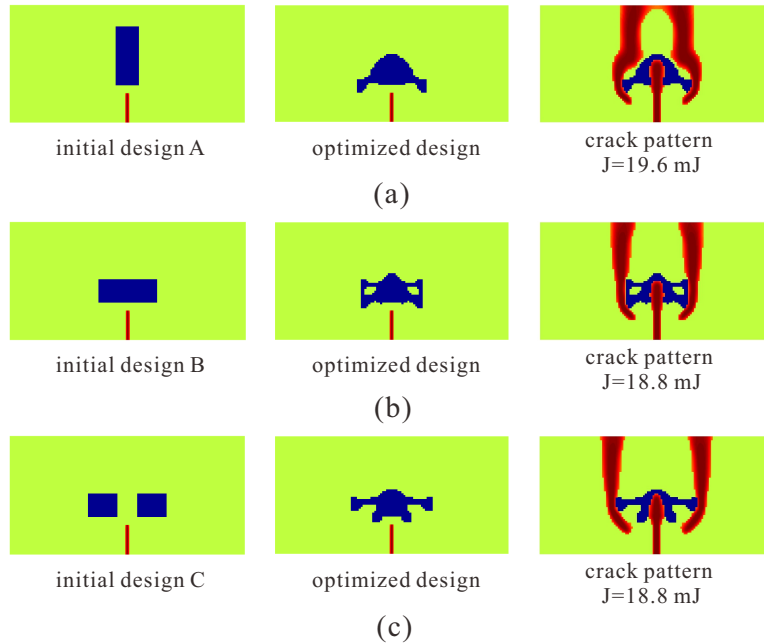


Figure 11: Influence of initial design on the optimized inclusion topologies using BESO method ($f^{inc} = 5\%$). Crack and inclusions are denoted by red and blue color, respectively.

From Fig. 12 and Fig. 13, we can conclude that even though SIMP has slightly better convergence properties with less oscillations, the convergence of both methods is comparable when an initial design is set such as the target volume fraction f^{inc} is met at the first iteration. The final results are also very close. The only difference is that starting from the target volume fraction f^{inc} is simpler with SIMP, as a value can be set in each element between 0 and 1, while in BESO an initial guess design matching the target volume fraction is required, which may be not trivial to define for more complex geometries. However, an initial homogeneous design is also possible using BESO, but the actual volume fraction will be changed at each iteration to reach f^{inc} as ρ_e in each element can only be 0 or 1. We investigate this case in Figs 12 and 13 (solution referred to as "homogeneous design, BESO": we can see that the convergence curve (Fig. 12) shows much more oscillations for BESO than SIMP for a homogeneous design, even though we can note in Fig. 13 that the optimized fracture energy is higher for BESO.

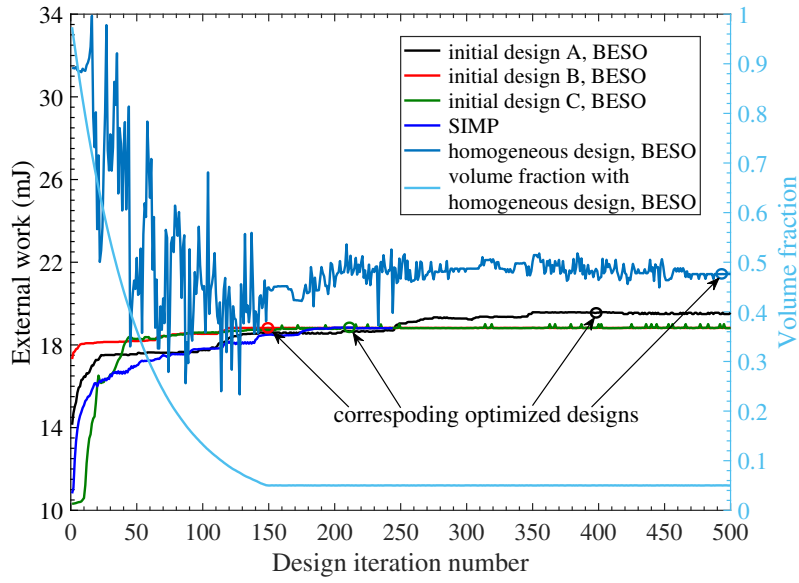


Figure 12: Convergence of the topology optimization scheme for BESO and SIMP schemes ($f^{inc} = 5\%$).

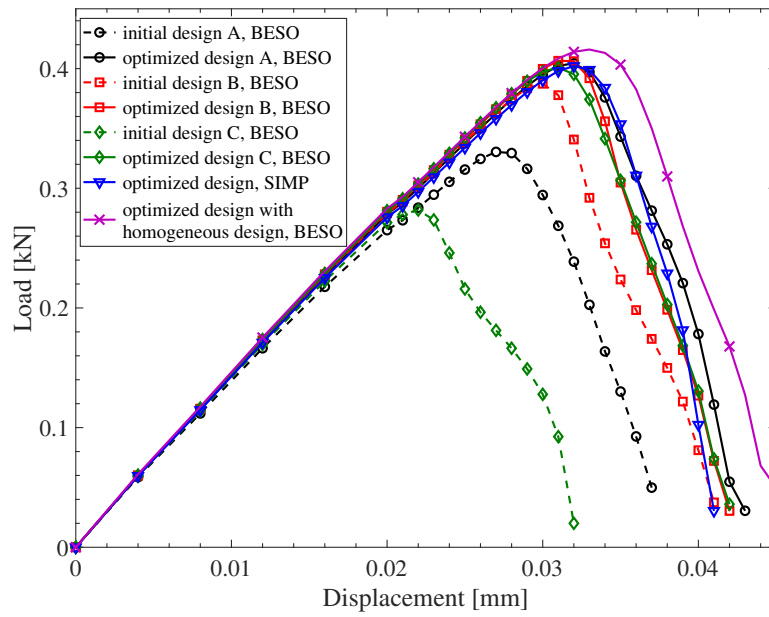


Figure 13: Load-displacement curves for initial and optimized designs ($f^{inc} = 5\%$).

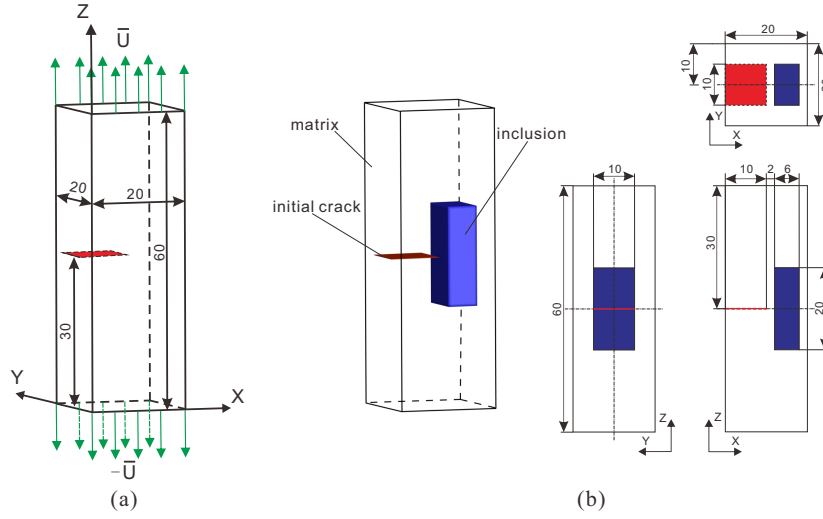


Figure 14: 3D sample with one pre-existing crack subjected to uniaxial tension: (a) geometry and boundary conditions; (b) guess design ($f^{inc} = 5\%$) using SIMP. Crack and inclusions are denoted by red and blue color, respectively.

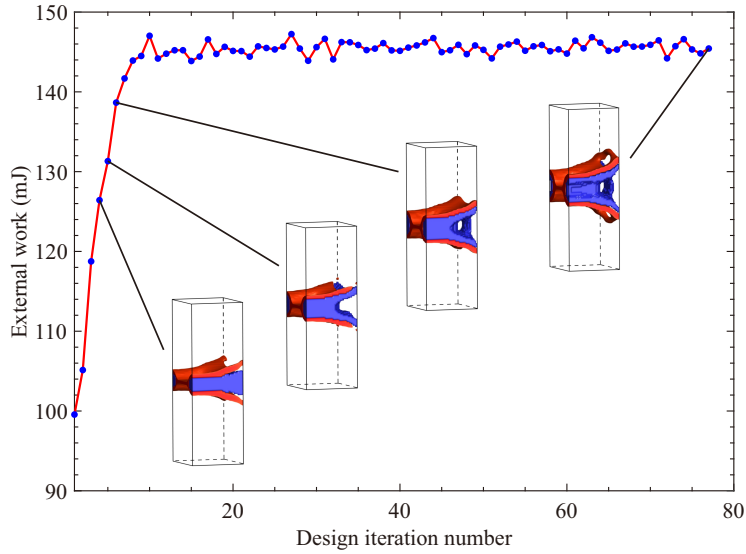


Figure 15: 3D sample with one pre-existing crack: evolution of inclusion topologies and associated final crack patterns ($f^{inc} = 5\%$). Crack and inclusions are denoted by red and blue color, respectively.

5.2. 3D reinforced sample with one pre-existing crack notch surface

In this example, the aim is to illustrate the applicability and convergence of the present method for 3D problems. For this purpose, a 3D sample with one pre-existing crack notch surface, as described in Fig. 14(a), is considered. The dimensions of the 3D sample are $20 \times 20 \times 60 \text{ mm}^3$. The domain is discretized into $40 \times 40 \times 120$ eight-node cubic elements. The dimensions of the pre-existing crack notch surface are $10 \times 10 \text{ mm}^2$. As in the 2D case of section 5.1, the pre-existing crack is modeled by prescribing Dirichlet conditions on the crack phase field with $d = 1$ along the

crack surface. On the upper and lower ends of the sample, vertical incremental displacement loads with $\Delta\bar{U} = 0.005$ mm are prescribed for the first four load increments and $\Delta\bar{U} = 0.002$ mm for the following load increments. Additionally, the optimality convergence tolerance is set at 10^{-5} ($tol = 10^{-5}$).

In Fig. 14(b) we provide a guess design for the inclusion, with $f^{inc} = 5\%$, corresponding to a simple parallelepipedic domain which will serve as a comparison with the SIMP optimized topology solution. Fig. 15 shows the evolution histories of inclusion topologies and their final crack patterns using SIMP. For 3D visualization purpose, only values of $\rho_e \geq \rho_{thr}$ are plotted in constant blue color (ρ_{thr} is a threshold value, defined to make sure elements with volume fraction around f^{inc} appear). Here the SIMP solution converges in roughly 10 iterations and strictly in 77 iterations. As a comparison, BESO with initial homogeneous design takes 150 iterations to reach $f^{inc} = 0.05$, showing the lower computational cost and better convergence of SIMP in this case. The final BESO topologies are not shown here to avoid too many figures. Different views of the optimized design using SIMP are shown in Fig. 16. Detailed propagation of the crack phase field corresponding to its load-displacement curve for the optimized design is shown in Fig. 17. It can be observed that the crack first initiates from the surface of the inclusion phase and then interacts with the pre-existing crack. Next, it propagates along the surface of the inclusion phase until crossing the whole domain and leading to the failure of the structure. Fig. 18 shows comparison of load-displacement curves and final crack patterns for guess and optimized design. Here, the fracture resistance of the optimized design is 20% higher as compared with the guess design.

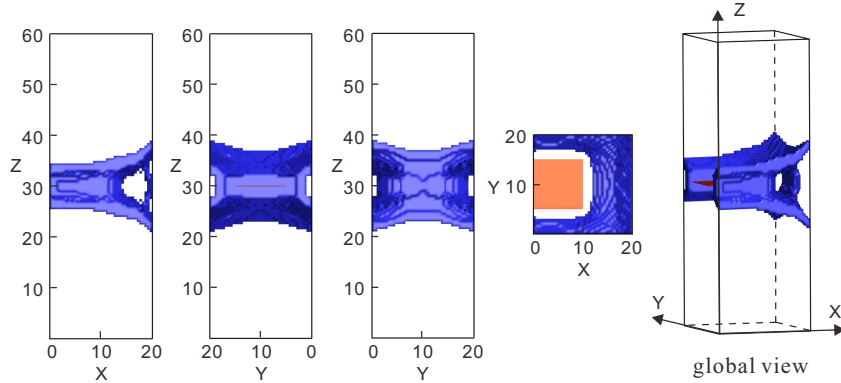


Figure 16: Different views of the optimized design of inclusion for the 3D sample with one pre-existing crack obtained by the SIMP formulation.

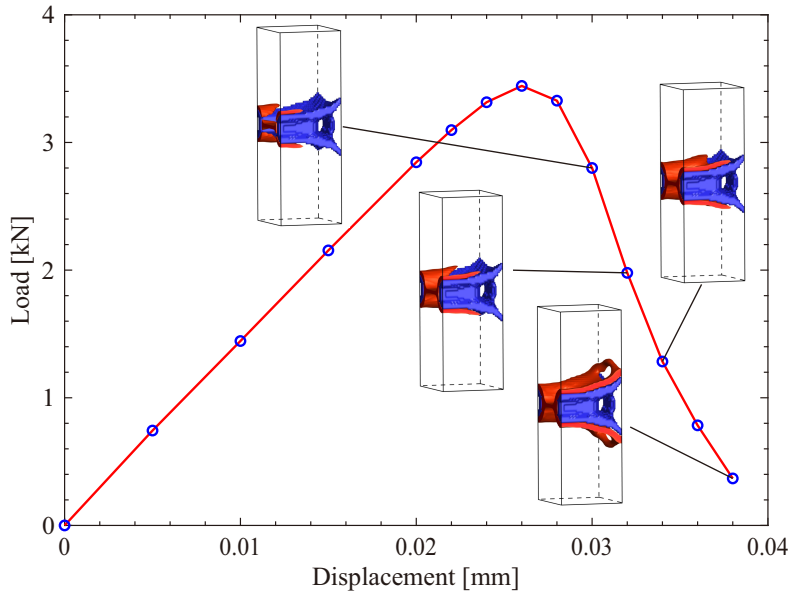


Figure 17: Load-displacement curve and crack evolution for the optimized design in the 3D sample with one pre-existing crack obtained by the SIMP formulation: (a) $\bar{U} = 0.03$ mm; (b) $\bar{U} = 0.032$ mm; (c) $\bar{U} = 0.034$ mm; (d) $\bar{U} = 0.038$ mm. Crack and inclusions are denoted by red and blue color, respectively.

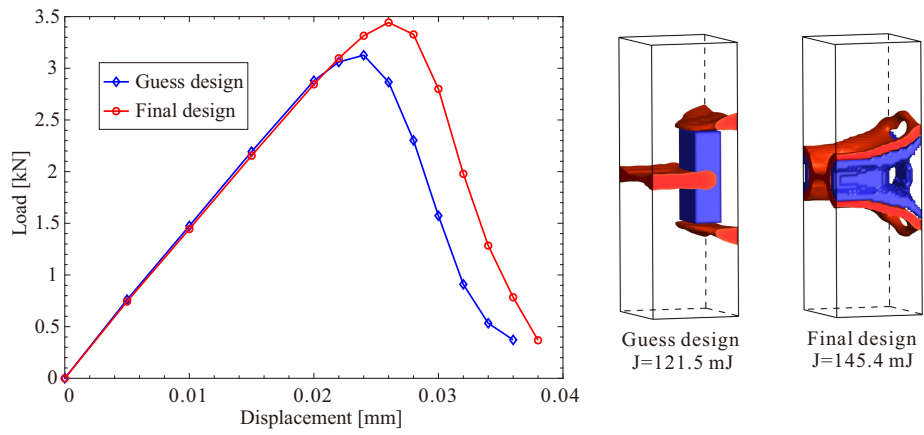


Figure 18: Load-displacement curves and final crack pattern for guess and optimized design in the 3D structure with one pre-existing crack obtained by the SIMP formulation. On the right figure, crack and inclusions are denoted by red and blue color, respectively.

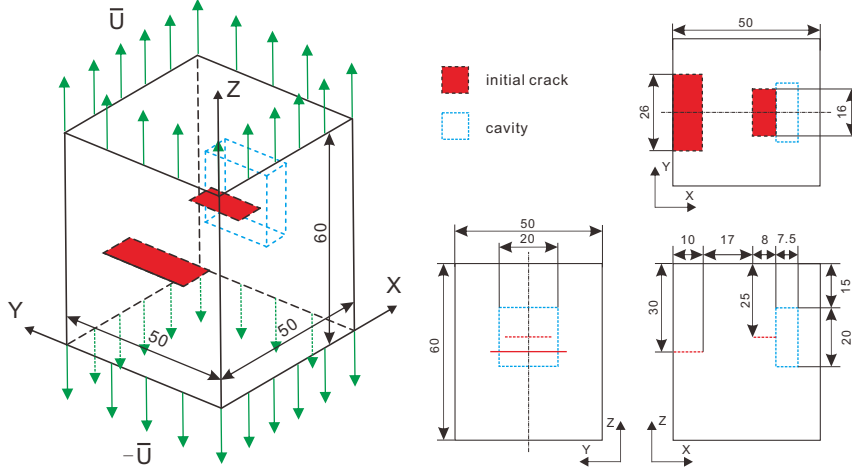


Figure 19: 3D sample with two pre-existing cracks and including parallelepipedic cavity: (a) geometry and boundary conditions.

5.3. 3D reinforced sample with two pre-existing crack surfaces and a parallelepipedic cavity

This final example demonstrates the potential of the method in complex 3D structural problems. The geometry and boundary conditions for this example are shown in Fig. 19. The dimensions of the 3D sample are $50 \times 50 \times 60 \text{ mm}^3$. The domain is discretized into $100 \times 100 \times 120$ eight-node cubic elements. As can be observed from Fig. 19, there are two pre-existing crack notch surfaces and a parallelepipedic cavity. The first pre-existing crack notch whose geometry is $26 \times 10 \text{ mm}^2$ is embedded in the left surface of the whole sample, the second pre-existing crack notch whose geometry is $16 \times 8 \text{ mm}^2$ is embedded in the left surface of the parallelepipedic cavity, and the parallelepipedic cavity whose geometry is $20 \times 20 \times 7.5 \text{ mm}^3$ is created by removing the elements at the position of the parallelepipedic cavity. Similar to the 3D case in section 5.2, the pre-existing cracks are simulated by prescribing Dirichlet conditions on the crack phase field with $d = 1$ along the crack surfaces. On the upper and lower ends of the sample, vertical incremental displacement loads with $\Delta \bar{U} = 0.005 \text{ mm}$ are prescribed with for the first four load increments and $\Delta \bar{U} = 0.002 \text{ mm}$ for the following load increments. Additionally, the optimality convergence tolerance is set at 10^{-3} ($tol = 10^{-3}$).

Fig. 20 shows the evolution histories of inclusion topologies and their final crack patterns. Here f^{inc} is set to 5%. As can be observed from Fig. 20, the inclusion material tends to accumulate around the pre-existing crack notch surfaces and the parallelepipedic cavity to prevent crack propagation and interaction in the sample. From Fig. 20, we can note that the SIMP solution is converged in roughly 12 iterations and strictly in 23 iterations. As a comparison, BESO with initial homogeneous design takes about 150 iterations to reach $f^{inc} = 0.05$, showing again much less computational costs and better convergence of SIMP in this case. Here again, BESO final designs are not shown for avoiding too many figures. For better visualization, different views of the optimized design are shown in Fig. 21. Detailed propagation of the crack phase field corresponding to its load-displacement curve for the optimal design is shown in Fig. 22. It can be observed that the cracks nucleate firstly at the two pre-existing crack notch surfaces and the corners of the cuboidal cavity, and then propagate and interact following the surface of the inclusion phase until reaching the fully broken state of the sample.

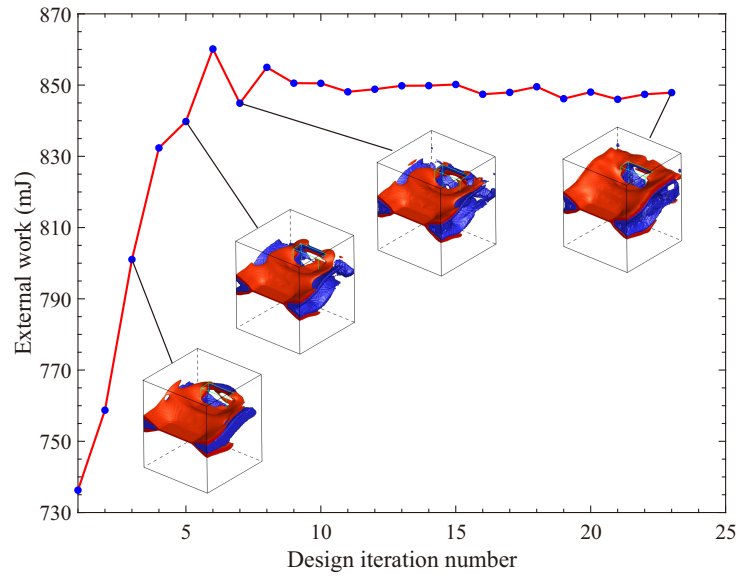


Figure 20: 3D sample with two pre-existing cracks: convergence of the topology optimization process, evolution of inclusion topologies and associated final crack patterns ($f^{inc} = 5\%$) obtained by the SIMP formulation. Crack and inclusions are denoted by red and blue color, respectively.

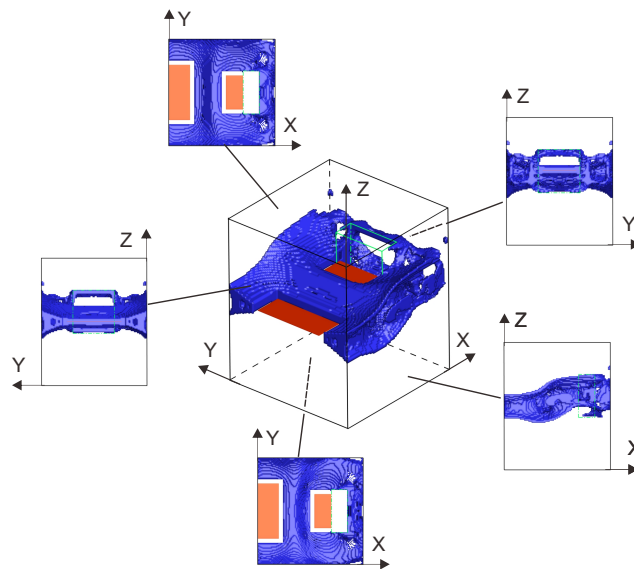


Figure 21: Different views of the optimized design for the 3D sample with two pre-existing cracks obtained by the SIMP formulation. Crack and inclusions are denoted by red and blue color, respectively.

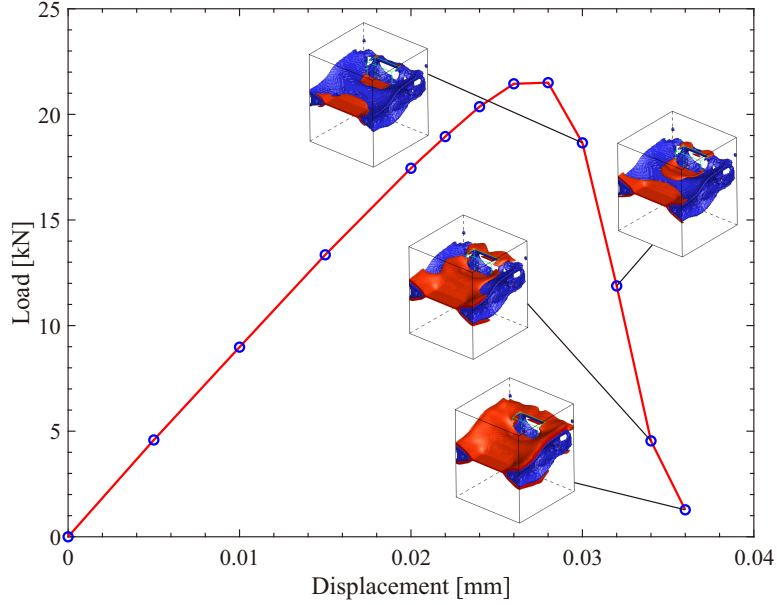


Figure 22: Load-displacement curves and crack pattern evolution for optimized design in the 3D structure with two pre-existing cracks obtained by the SIMP formulation: (a) $\bar{U} = 0.03$ mm; (b) $\bar{U} = 0.032$ mm; (c) $\bar{U} = 0.034$ mm; (d) $\bar{U} = 0.036$ mm. Crack and inclusions are denoted by red and blue color, respectively.

Table 3: Computational times for the different examples

Problem	No. elements	No. design iterations	Average CPU time (s)	Total simulation time (h)
2D reinforced plate ($f^{inc} = 5\%$)	7200	244	33.6	2.28
3D reinforced sample in 5.2	192,000	77	924	19.77
3D reinforced sample in 5.3	1,176,000	23	5055	32.3

5.4. Computational times

Finally, a summary of the computational times for the different examples is reported in Table 3. In this work, a workstation with 4 cores, 16 Go Ram and 3.00 GHz processor was used for all 2D cases. For all 3D cases, a workstation with 24 cores, 768 Go Ram and 2.70 GHz processor was used. The present code has been implemented in Matlab[®].

6. Conclusion

In this work, we proposed a framework employing SIMP topology optimization and phase field method to fracture to maximize the fracture resistance of composites (two-phase materials)

structures. The method allows taking into account the whole fracture process, from initiation to complete failure of the specimen. The continuous density representation of density obtained by the SIMP method allows a good convergence of the scheme and to improve the fracture resistance of a structure embedding a reinforcement phase (inclusion) for a fixed volume fraction.

We have observed that even though SIMP has slightly better convergence properties with less oscillations than BESO, the convergence of both SIMP and BESO is comparable when the initial volume fraction is set by an appropriate initial design in BESO. The final results are also very close. However, it is not always easy to define such initial design, especially in 3D. When using a homogeneous design with BESO, the convergence can be much slower (up to 6 times in some examples) than SIMP, as the actual volume fraction will be changed at each iteration by removing/adding material in each element. Then, starting with an initial homogeneous design is straightforward and leads to faster convergence with the present SIMP framework than with BESO.

This has been illustrated by conducting 3D applications in complex configurations, where defining an initial design with a given volume fraction may be non-trivial. Then, the present SIMP-phase field framework is a good candidate for reducing the computational times in designing materials and structures with enhanced fracture energy. An extension to interfacial damage interacting with bulk fracture has been proposed in [20, 21] and could be straightforwardly applied to the present SIMP framework. Another exciting perspective for this work would be to produce such bi-materials with optimized geometries and validate experimentally the numerical predictions.

Appendix: Finite Element discretization

The weak form of the mechanical problem can be found in (20). Using (28), we can re-write the associated weak form for the damage problem (21) as: find $d(\mathbf{x}) \in \mathcal{S}_d$, $\mathcal{S}_d = \{d|d(\mathbf{x}) = 1 \text{ on } \Gamma, d \in H^1(\Omega)\}$:

$$R_2 = \int_{\Omega} \{(\mathcal{H} + \psi_c) d \delta d + \psi_c \ell^2 \nabla d \cdot \nabla (\delta d)\} d\Omega - \int_{\Omega} \mathcal{H} \delta d d\Omega = 0. \quad (59)$$

and $\delta d(\mathbf{x}) \in \mathcal{S}_d^0$, $\mathcal{S}_d^0 = \{\delta d | \delta d(\mathbf{x}) = 0 \text{ on } \partial\Omega, d \in H^1(\Omega)\}$. In this work, we adopt the same finite element discretization for the approximation of the crack phase field d and the displacement field \mathbf{u} . We can express the discretization of the phase field problem as:

$$d = \mathbf{N}_d \mathbf{d}_e, \quad \nabla d = \mathbf{B}_d \mathbf{d}_e, \quad (60)$$

where \mathbf{N}_d and \mathbf{B}_d are matrices of damage shape function and of damage shape function derivatives, respectively, and \mathbf{d}_e denote nodal damage in one element. The discretization of damage problem (59) results into the following discrete system of equations:

$$\mathbf{K}_d \mathbf{d} = \mathbf{F}_d \quad (61)$$

in which

$$\mathbf{K}_d = \int_{\Omega} \{[\mathcal{H} + \psi_c] \mathbf{N}_d^T \mathbf{N}_d + \psi_c \ell^2 \mathbf{B}_d^T \mathbf{B}_d\} d\Omega \quad (62)$$

and

$$\mathbf{F}_d = \int_{\Omega} \mathbf{N}_d^T \mathcal{H} d\Omega, \quad (63)$$

where \mathcal{H} is given in (26). The displacement problem can be discretized as:

$$\mathbf{u} = \mathbf{N}_u \mathbf{u}_e, \quad \delta \mathbf{u} = \mathbf{N}_u \delta \mathbf{u}_e, \quad [\boldsymbol{\varepsilon}] (\mathbf{u}) = \mathbf{B}_u \mathbf{u}_e, \quad [\boldsymbol{\varepsilon}] (\delta \mathbf{u}) = \mathbf{B}_u \delta \mathbf{u}_e \quad (64)$$

where \mathbf{u}_e , \mathbf{N}_u and \mathbf{B}_u are nodal displacement components in one element, a matrix of displacement shape function and a matrix of displacement shape function derivatives, respectively. Using the weak form (20), we obtain the following discrete system of equations:

$$\mathbf{K}_u \mathbf{u} = \mathbf{F}_u \quad (65)$$

with the force vector

$$\mathbf{F}_u = \int_{\Omega} \mathbf{N}_u^T \mathbf{f} d\Omega + \int_{\partial\Omega_F} \mathbf{N}_u^T \mathbf{F} dS \quad (66)$$

and the stiffness matrix

$$\mathbf{K}_u = \int_{\Omega} \mathbf{B}_u^T \underbrace{\left[(1-d)^2 \left(\lambda R^+ [\mathbf{1}] [\mathbf{1}]^T + 2\mu \mathbf{P}^+ \right) + \left(\lambda R^- [\mathbf{1}] [\mathbf{1}]^T + 2\mu \mathbf{P}^- \right) \right]}_{\frac{\partial[\boldsymbol{\sigma}]}{\partial[\boldsymbol{\varepsilon}]}} \mathbf{B}_u d\Omega \quad (67)$$

where $[\boldsymbol{\sigma}]$ and $[\boldsymbol{\varepsilon}]$ are the vector forms corresponding to the second order tensors of stress $\boldsymbol{\sigma}$ and strain $\boldsymbol{\varepsilon}$. R^\pm and \mathbf{P}^\pm are two operators for the decomposition of strain into the tensile and compressive parts (see [49] for more details) and \mathbf{P}^\pm are the matrix forms corresponding to the fourth order projection tensor $\mathbb{P}^\pm = \frac{\partial \boldsymbol{\varepsilon}^\pm}{\partial \boldsymbol{\varepsilon}}$, which can be found in [5, 40].

Acknowledgements

This work has benefited from the project "Multiscale Modeling and Experimental Investigation of damage in composite components obtained by additive manufacturing process" (MMELED), ANR-16-CE08-0044-04. Yi Wu gratefully acknowledged the support from China Scholarship Council (CSC No. 201906130024).

Conflict of interest statement

On behalf of all authors, the corresponding author states that there is no conflict of interest.

References

- [1] Roberto Alessi. *Variational approach to fracture mechanics with plasticity*. PhD thesis, Ecole Polytechnique X, 2013.
- [2] Roberto Alessi, Jean-Jacques Marigo, and Stefano Vidoli. Gradient damage models coupled with plasticity: variational formulation and main properties. *Mechanics of Materials*, 80:351–367, 2015.
- [3] Grégoire Allaire, François Jouve, and Anca-Maria Toader. Structural optimization using sensitivity analysis and a level-set method. *Journal of computational physics*, 194(1):363–393, 2004.
- [4] M. Ambati, T. Gerasimov, and L. de Lorenzis. A review on phase-field models of brittle fracture and a new fast hybrid formulation. *Computational Mechanics*, 55(2):383–405, 2015.
- [5] Marreddy Ambati. *Phase-field Modeling and Computations of Brittle and Ductile Fracture for Solids and Shells*. Technische Universität Carolo-Wilhelmina zu Braunschweig, 2017.
- [6] Luigi Ambrosio and Vincenzo Maria Tortorelli. Approximation of functional depending on jumps by elliptic functional via t-convergence. *Communications on Pure and Applied Mathematics*, 43(8):999–1036, 1990.

- [7] Anish Ravindra Amin, Yi-Tang Kao, Bruce L Tai, and Jyhwen Wang. Dynamic response of 3d-printed bi-material structure using drop weight impact test. In *International Manufacturing Science and Engineering Conference*, volume 50732, page V002T01A021. American Society of Mechanical Engineers, 2017.
- [8] Oded Amir. A topology optimization procedure for reinforced concrete structures. *Computers & Structures*, 114:46–58, 2013.
- [9] Oded Amir and Ole Sigmund. Reinforcement layout design for concrete structures based on continuum damage and truss topology optimization. *Structural and Multidisciplinary Optimization*, 47(2):157–174, 2013.
- [10] Hanen Amor, Jean-Jacques Marigo, and Corrado Maurini. Regularized formulation of the variational brittle fracture with unilateral contact: Numerical experiments. *Journal of the Mechanics and Physics of Solids*, 57(8):1209–1229, 2009.
- [11] Erik Andreassen, Anders Clausen, Mattias Schevenels, Boyan S Lazarov, and Ole Sigmund. Efficient topology optimization in matlab using 88 lines of code. *Structural and Multidisciplinary Optimization*, 43(1):1–16, 2011.
- [12] Martin P Bendsøe. Optimal shape design as a material distribution problem. *Structural optimization*, 1(4):193–202, 1989.
- [13] Martin P Bendsøe and Ole Sigmund. Material interpolation schemes in topology optimization. *Archive of applied mechanics*, 69(9-10):635–654, 1999.
- [14] Martin Philip Bendsoe and Noboru Kikuchi. Generating optimal topologies in structural design using a homogenization method. 1988.
- [15] MP Bendsøe and O Sigmund. Theory, methods and applications. *Topology optimization*. Springer, Berlin, 2003.
- [16] M.J. Borden, C.V. Verhoosel, M.A. Scott, T.J.R. Hughes, and C.M. Landis. A phase-field description of dynamic brittle fracture. *Computer Methods in Applied Mechanics and Engineering*, 217:77–95, 2012.
- [17] B. Bourdin, G.A. Francfort, and J.J. Marigo. *The Variational Approach to Fracture*. Springer-Verlag, Berlin, 2008.
- [18] Thomas Buhl, Claus BW Pedersen, and Ole Sigmund. Stiffness design of geometrically nonlinear structures using topology optimization. *Structural and Multidisciplinary Optimization*, 19(2):93–104, 2000.
- [19] Vivien J Challis, Anthony P Roberts, and Andrew H Wilkins. Fracture resistance via topology optimization. *Structural and Multidisciplinary Optimization*, 36(3):263–271, 2008.
- [20] Daicong Da and Julien Yvonnet. Topology optimization for maximizing the fracture resistance of periodic quasi-brittle composites structures. *Materials*, 13(15):3279, 2020.
- [21] Daicong Da, Julien Yvonnet, Liang Xia, and Guangyao Li. Topology optimization of particle-matrix composites for optimal fracture resistance taking into account interfacial damage. *International Journal for Numerical Methods in Engineering*, 115(5):604–626, 2018.
- [22] Joshua D Deaton and Ramana V Grandhi. A survey of structural and multidisciplinary continuum topology optimization: post 2000. *Structural and Multidisciplinary Optimization*, 49(1):1–38, 2014.
- [23] Gilles A Francfort and J-J Marigo. Revisiting brittle fracture as an energy minimization problem. *Journal of the Mechanics and Physics of Solids*, 46(8):1319–1342, 1998.
- [24] T Guillén-Hernández, IG García, J Reinoso, and M Paggi. A micromechanical analysis of inter-fiber failure in long reinforced composites based on the phase field approach of fracture combined with the cohesive zone model. *International Journal of Fracture*, 220(2):181–203, 2019.
- [25] T Guillén-Hernández, A Quintana-Corominas, IG García, J Reinoso, M Paggi, and A Turón. In-situ strength effects in long fibre reinforced composites: A micro-mechanical analysis using the phase field approach of fracture. *Theoretical and Applied Fracture Mechanics*, 108:102621, 2020.
- [26] Carl Frédéric Hilchenbach and Ekkehard Ramm. Optimization of multiphase structures considering damage. *Structural and Multidisciplinary Optimization*, 51(5):1083–1096, 2015.
- [27] X Huang and YM Xie. Convergent and mesh-independent solutions for the bi-directional evolutionary structural optimization method. *Finite Elements in Analysis and Design*, 43(14):1039–1049, 2007.
- [28] Kai A James and Haim Waisman. Failure mitigation in optimal topology design using a coupled nonlinear continuum damage model. *Computer Methods in Applied Mechanics and Engineering*, 268:614–631, 2014.
- [29] Zhan Kang, Pai Liu, and Ming Li. Topology optimization considering fracture mechanics behaviors at specified locations. *Structural and Multidisciplinary Optimization*, 55(5):1847–1864, 2017.
- [30] Yi-Tang Kao, Anish Ravindra Amin, Nolan Payne, Jyhwen Wang, and Bruce L Tai. Low-velocity impact response of 3d-printed lattice structure with foam reinforcement. *Composite Structures*, 192:93–100, 2018.
- [31] Yi-Tang Kao, Ying Zhang, Jyhwen Wang, and Bruce L Tai. Loading-unloading cycles of 3d-printing built bi-material structures with ceramic and elastomer. In *International Manufacturing Science and Engineering Conference*, volume 49910, page V003T08A008. American Society of Mechanical Engineers, 2016.
- [32] Yi-Tang Kao, Ying Zhang, Jyhwen Wang, and Bruce L Tai. Bending behaviors of 3d-printed bi-material

- structure: Experimental study and finite element analysis. *Additive Manufacturing*, 16:197–205, 2017.
- [33] Junji Kato and Ekkehard Ramm. Multiphase layout optimization for fiber reinforced composites considering a damage model. *Engineering structures*, 49:202–220, 2013.
- [34] Lei Li and Kapil Khandelwal. Design of fracture resistant energy absorbing structures using elastoplastic topology optimization. *Structural and Multidisciplinary Optimization*, 56(6):1447–1475, 2017.
- [35] Lei Li, Guodong Zhang, and Kapil Khandelwal. Topology optimization of energy absorbing structures with maximum damage constraint. *International Journal for Numerical Methods in Engineering*, 112(7):737–775, 2017.
- [36] Lei Li, Guodong Zhang, and Kapil Khandelwal. Failure resistant topology optimization of structures using nonlocal elastoplastic-damage model. *Structural and Multidisciplinary Optimization*, 58(4):1589–1618, 2018.
- [37] Pengfei Li, Julien Yvonnet, and Christelle Combescure. An extension of the phase field method to model interactions between interfacial damage and brittle fracture in elastoplastic composites. *International Journal of Mechanical Sciences*, page 105633, 2020.
- [38] Pai Liu, Yangjun Luo, and Zhan Kang. Multi-material topology optimization considering interface behavior via xfem and level set method. *Computer methods in applied mechanics and engineering*, 308:113–133, 2016.
- [39] Christian Miehe, Martina Hofacker, and Fabian Welschinger. A phase field model for rate-independent crack propagation: Robust algorithmic implementation based on operator splits. *Computer Methods in Applied Mechanics and Engineering*, 199(45-48):2765–2778, 2010.
- [40] Christian Miehe and Matthias Lambrecht. Algorithms for computation of stresses and elasticity moduli in terms of seth–hill’s family of generalized strain tensors. *Communications in numerical methods in engineering*, 17(5):337–353, 2001.
- [41] Christian Miehe, Lisa-Marie Schaezel, and Heike Ulmer. Phase field modeling of fracture in multi-physics problems. part i. balance of crack surface and failure criteria for brittle crack propagation in thermo-elastic solids. *Computer Methods in Applied Mechanics and Engineering*, 294:449–485, 2015.
- [42] Christian Miehe, Fabian Welschinger, and Martina Hofacker. Thermodynamically consistent phase-field models of fracture: Variational principles and multi-field fe implementations. *International Journal for Numerical Methods in Engineering*, 83(10):1273–1311, 2010.
- [43] Alexander Mielke. Evolution of rate-independent systems. *Evolutionary equations*, 2:461–559, 2005.
- [44] Alexander Mielke. A mathematical framework for generalized standard materials in the rate-independent case. In *Multifield Problems in Solid and Fluid Mechanics*, pages 399–428. Springer, 2006.
- [45] Gergely Molnár, Aurélien Doitrand, Rafaël Estevez, and Anthony Gravouil. Toughness or strength? regularization in phase-field fracture explained by the coupled criterion. *Theoretical and Applied Fracture Mechanics*, page 102736, 2020.
- [46] Tuan D Ngo, Alireza Kashani, Gabriele Imbalzano, Kate TQ Nguyen, and David Hui. Additive manufacturing (3d printing): A review of materials, methods, applications and challenges. *Composites Part B: Engineering*, 143:172–196, 2018.
- [47] Thanh Tung Nguyen, Julien Yvonnet, Michel Bornert, and Camille Chateau. Initiation and propagation of complex 3d networks of cracks in heterogeneous quasi-brittle materials: Direct comparison between in situ testing-microct experiments and phase field simulations. *Journal of the Mechanics and Physics of Solids*, 95:320–350, 2016.
- [48] Thanh Tung Nguyen, Julien Yvonnet, Michel Bornert, Camille Chateau, Karam Sab, R Romani, and Robert Le Roy. On the choice of parameters in the phase field method for simulating crack initiation with experimental validation. *International Journal of Fracture*, 197(2):213–226, 2016.
- [49] Thanh Tung Nguyen, Julien Yvonnet, Q-Z Zhu, Michel Bornert, and Camille Chateau. A phase field method to simulate crack nucleation and propagation in strongly heterogeneous materials from direct imaging of their microstructure. *Engineering Fracture Mechanics*, 139:18–39, 2015.
- [50] Thanh Tung Nguyen, Julien Yvonnet, Q-Z Zhu, Michel Bornert, and Camille Chateau. A phase-field method for computational modeling of interfacial damage interacting with crack propagation in realistic microstructures obtained by microtomography. *Computer Methods in Applied Mechanics and Engineering*, 312:567–595, 2016.
- [51] Kim Pham, Jean-Jacques Marigo, and Corrado Maurini. The issues of the uniqueness and the stability of the homogeneous response in uniaxial tests with gradient damage models. *Journal of the Mechanics and Physics of Solids*, 59(6):1163–1190, 2011.
- [52] George IN Rozvany. A critical review of established methods of structural topology optimization. *Structural and multidisciplinary optimization*, 37(3):217–237, 2009.
- [53] George IN Rozvany, Ming Zhou, and Torben Birker. Generalized shape optimization without homogenization. *Structural optimization*, 4(3-4):250–252, 1992.

- [54] Jonathan B Russ and Haim Waisman. A novel topology optimization formulation for enhancing fracture resistance with a single quasi-brittle material. *International Journal for Numerical Methods in Engineering*.
- [55] Jonathan B Russ and Haim Waisman. Topology optimization for brittle fracture resistance. *Computer Methods in Applied Mechanics and Engineering*, 347:238–263, 2019.
- [56] Bingbing San and Haim Waisman. Optimization of carbon black polymer composite microstructure for rupture resistance. *Journal of Applied Mechanics*, 84(2), 2017.
- [57] Karlo Seleš, Ante Jurčević, Zdenko Tonković, and Jurica Sorić. Crack propagation prediction in heterogeneous microstructure using an efficient phase-field algorithm. *Theoretical and Applied Fracture Mechanics*, 100:289–297, 2019.
- [58] Ole Sigmund. A 99 line topology optimization code written in matlab. *Structural and multidisciplinary optimization*, 21(2):120–127, 2001.
- [59] Ole Sigmund and Kurt Maute. Topology optimization approaches. *Structural and Multidisciplinary Optimization*, 48(6):1031–1055, 2013.
- [60] Krister Svanberg. The method of moving asymptotes a new method for structural optimization. *International journal for numerical methods in engineering*, 24(2):359–373, 1987.
- [61] Nico P van Dijk, Kurt Maute, Matthijs Langelaar, and Fred Van Keulen. Level-set methods for structural topology optimization: a review. *Structural and Multidisciplinary Optimization*, 48(3):437–472, 2013.
- [62] Michael Yu Wang, Xiaoming Wang, and Dongming Guo. A level set method for structural topology optimization. *Computer methods in applied mechanics and engineering*, 192(1-2):227–246, 2003.
- [63] Xin Wang, Man Jiang, Zuowan Zhou, Jihua Gou, and David Hui. 3d printing of polymer matrix composites: A review and prospective. *Composites Part B: Engineering*, 110:442–458, 2017.
- [64] Chi Wu, Jianguang Fang, Shiwei Zhou, Grant Steven, and Qing Li. Level-set topology optimization for maximizing fracture resistance of brittle materials using phase field fracture model. *accepted*.
- [65] Jian-Ying Wu and Yuli Huang. Comprehensive implementations of phase-field damage models in abaqus. *Theoretical and Applied Fracture Mechanics*, 106:102440, 2020.
- [66] Liang Xia, Daicong Da, and Julien Yvonnet. Topology optimization for maximizing the fracture resistance of quasi-brittle composites. *Computer Methods in Applied Mechanics and Engineering*, 332:234–254, 2018.
- [67] Yi M Xie and Grant P Steven. A simple evolutionary procedure for structural optimization. *Computers & structures*, 49(5):885–896, 1993.
- [68] Xue Zhang, Chet Vignes, Scott W Sloan, and Daichao Sheng. Numerical evaluation of the phase-field model for brittle fracture with emphasis on the length scale. *Computational Mechanics*, 59(5):737–752, 2017.
- [69] Zhongpu Zhang, Junning Chen, Eric Li, Wei Li, Michael Swain, and Qing Li. Topological design of all-ceramic dental bridges for enhancing fracture resistance. *International journal for numerical methods in biomedical engineering*, 32(6):e02749, 2016.
- [70] Shuwei Zhou, Xiaoying Zhuang, Hehua Zhu, and Timon Rabczuk. Phase field modelling of crack propagation, branching and coalescence in rocks. *Theoretical and Applied Fracture Mechanics*, 96:174–192, 2018.
- [71] Ji-Hong Zhu, Wei-Hong Zhang, and Liang Xia. Topology optimization in aircraft and aerospace structures design. *Archives of Computational Methods in Engineering*, 23(4):595–622, 2016.